

## RESEARCH ARTICLE

10.1029/2018JD028994

## Key Points:

- Diurnal variation of boundary layer ozone was measured using tethered-balloon platform for a multiday ozone episode in Nanjing, east China
- Agricultural biomass burning influenced ozone concentration in the free troposphere and within boundary layer in the downwind region
- Vertical mixing of aged urban plumes from the residual layer significantly influences morning surface ozone and daytime ozone buildup

## Supporting Information:

- Supporting Information S1
- Data Set S1

## Correspondence to:

X. Huang and A. Ding,  
xinhuang@nju.edu.cn;  
dingaj@nju.edu.cn

## Citation:

Xu, Z., Huang, X., Nie, W., Shen, Y., Zheng, L., Xie, Y., et al. (2018). Impact of biomass burning and vertical mixing of residual-layer aged plumes on ozone in the Yangtze River Delta, China: A tethered-balloon measurement and modeling study of a multiday ozone episode. *Journal of Geophysical Research: Atmospheres*, 123, 11,786–11,803. <https://doi.org/10.1029/2018JD028994>

Received 13 MAY 2018

Accepted 24 SEP 2018

Accepted article online 3 OCT 2018

Published online 30 OCT 2018




## Author Contributions:

**Conceptualization:** Aijun Ding**Data curation:** Zhengning Xu, Wei Nie, Yicheng Shen, Longfei Zheng, Yuning Xie, Ximeng Qi**Formal analysis:** Zhengning Xu, Tianyi Wang**Investigation:** Aijun Ding**Methodology:** Zhengning Xu, Xin Huang, Ke Ding, Lixia Liu, Derong Zhou, Ximeng Qi**Resources:** Aijun Ding**Supervision:** Aijun Ding**Validation:** Xin Huang**Visualization:** Zhengning Xu, Xin Huang, Tianyi Wang, Ke Ding, Lixia Liu, Derong Zhou

(continued)

©2018. American Geophysical Union.  
All Rights Reserved.

## Impact of Biomass Burning and Vertical Mixing of Residual-Layer Aged Plumes on Ozone in the Yangtze River Delta, China: A Tethered-Balloon Measurement and Modeling Study of a Multiday Ozone Episode

Zhengning Xu<sup>1,2</sup>, Xin Huang<sup>1,2</sup> , Wei Nie<sup>1,2</sup>, Yicheng Shen<sup>1</sup> , Longfei Zheng<sup>1</sup>, Yuning Xie<sup>1</sup>, Tianyi Wang<sup>1</sup>, Ke Ding<sup>1</sup>, Lixia Liu<sup>1,3</sup>, Derong Zhou<sup>1</sup>, Ximeng Qi<sup>1,2</sup>, and Aijun Ding<sup>1,2</sup> 

<sup>1</sup>Joint International Research Laboratory of Atmospheric and Earth System Sciences, School of Atmospheric Sciences, Nanjing University, Nanjing, China, <sup>2</sup>Jiangsu Provincial Collaborative Innovation Center for Climate Change, Nanjing, China, <sup>3</sup>Now at Max Planck Institute for Chemistry, Mainz, Germany

**Abstract** Ozone (O<sub>3</sub>) is one of the most important trace gases in the troposphere because of its impact on human health, crop yield, climate change, and atmospheric oxidizing capacity. In recent years, China has suffered from deleterious O<sub>3</sub> pollution in many regions, especially in eastern China during summer. However, understanding the causes of high O<sub>3</sub> pollution episodes is still limited because existing measurements were mainly conducted at the surface level. In this study, we conducted an intensive tethered-balloon measurement at the Station for Observing Regional Processes of the Earth System in the Yangtze River Delta during a multiday O<sub>3</sub> episode in mid-June 2014, with the highest hourly surface O<sub>3</sub> record (142 ppbv) at the station in 2014. By integrating available ground-based, remote sensing and aircraft measurement data together with chemical transport modeling and Lagrangian dispersion modeling, we carried out a comprehensive analysis of the main source and formation mechanism for two typical days during the multiday O<sub>3</sub> episode. On 11 June, agricultural straw burning in the north significantly enhanced O<sub>3</sub> concentration (40–50 ppbv) above the planetary boundary layer (PBL) over Nanjing and further influenced the downwind surface O<sub>3</sub> in the following days. On 14 June, regional photochemically aged air masses from city clusters in the Yangtze River Delta substantially influenced early morning ground O<sub>3</sub> concentrations by vertical mixing from the residual layer and contributed to PBL daytime O<sub>3</sub> buildup. This study provides a clear picture of the transport and mixing of O<sub>3</sub> and relevant pollutants in the PBL from different sources and highlights the significance of regional emission control in the mitigation of photochemical pollution in eastern China.

**Plain Language Summary** Ozone pollution is one the important air quality concerns in China, especially in early summer. The causes of high ozone pollution events are poorly understood because of less information about the vertical profiles. Here we conducted intensive measurement of ozone with a tethered-balloon platform in Nanjing, a city in the western Yangtze River Delta, China during a multi-day ozone episode in mid-June 2014. Highest hourly surface ozone record (142 ppbv) in 2014 was observed at that day. Various measurement data from ground-based, remote sensing and aircraft platforms during the same period, and numerical modeling with two different models were conducted to understand the mechanisms and causes during this event. We found that agricultural straw burning has strong impact on ozone concentrations in the free troposphere of eastern China and ground surface in the downwind area. The vertical mixing of aged "city" plumes in the residual-layer had important influence on the fast increase of surface ozone in the morning and the daytime buildup. Our study gives a clearer picture about the transport and mixing of ozone and relevant pollutants in the boundary layer from different sources, and highlights the significance of regional emission control in mitigation of photochemical pollution in eastern China.

### 1. Introduction

Ozone (O<sub>3</sub>) pollution is one of the important air quality concerns because of its negative impact on human health and agricultural yields (Carter et al., 2017; Crawford et al., 1997; Fishman et al., 1979; Fleming et al., 2018; Fuhrer et al., 1997; McKee, 1994; Schultz et al., 2017). O<sub>3</sub> has a relatively long lifetime, from several days

**Writing - original draft:** Zhengning Xu  
**Writing - review & editing:** Xin Huang,  
Wei Nie, Aijun Ding

to weeks, in the atmosphere (Fishman et al., 1979; Fleming et al., 2018). The O<sub>3</sub> concentration at the ground surface is influenced not only by chemical processes (W. Lin et al., 2011; Xue et al., 2014; R. Wang, Xu, et al., 2017; T. Wang, Xue, et al., 2017) but also by transport in the planetary boundary layer (PBL) at multiple scales (Corsmeier et al., 1997; Ding et al., 2008; C. H. Lin et al., 2006; Mazzuca et al., 2017; Pollack et al., 2012; Reitebuch et al., 2000; Schnell et al., 2016; Velasco et al., 2008; R. Wang, Xu, et al., 2017; T. Wang, Xue, et al., 2017; J. Zhang & Rao, 1999). Therefore, measurements of the spatiotemporal variations, especially in the vertical profiles, of O<sub>3</sub> and relevant parameters in the PBL are very important for improving the understanding of the causes of O<sub>3</sub> pollution and for taking appropriate control measures to mitigate O<sub>3</sub> pollution in a specific region.

Coastal China is one of the main regions experiencing increasing O<sub>3</sub> both at the surface and in the lower troposphere (Ding et al., 2008; Sun et al., 2016; T. Wang et al., 2009; X. Xu et al., 2008), in contrast with many other regions in the world (Cooper et al., 2010; Ding et al., 2008; Fleming et al., 2018). In recent years, O<sub>3</sub> pollution has become the most important concern for summertime air quality in many city cluster regions, such as the Beijing-Tianjin Area, the Yangtze River Delta (YRD), and the Pearl River Delta (C. K. Chan & Yao, 2008; R. Wang, Xu, et al., 2017; T. Wang, Xue, et al., 2017). However, only a limited number of studies have focused on the vertical distribution of O<sub>3</sub> and its precursors in these developed regions. For example, Ding et al. (2008) analyzed the climatology of tropospheric O<sub>3</sub> over Beijing and the surrounding areas based on in-service airlines of the Water Vapor by Airbus In-Service Aircraft (MOZAIC) program from 1995 to 2005, and showed the first picture of PBL O<sub>3</sub> structure, and reported a significant positive PBL O<sub>3</sub> trend in northern China. R. Wang, Xu, et al. (2017) conducted unmanned aerial vehicle measurements of O<sub>3</sub> and aerosols in a city in the North China Plain and compared them with MOZAIC measurements in Beijing. Y. Wang et al. (2012) reported the climatological distribution and trend of tropospheric O<sub>3</sub> based on ozonesonde measurements over Beijing. Long-term ozonesonde studies were also performed in Hong Kong in the Pearl River Delta region in South China (C. Y. Chan et al., 2003; Zhou et al., 2013), and the main sources of O<sub>3</sub> at different altitudes of the troposphere were discussed (Zhou et al., 2013). However, among these studies, only aircraft measurements from Beijing provided a clear picture of the diurnal variation of O<sub>3</sub> concentration in the PBL (Ding et al., 2008).

The YRD region, which includes several megacities such as Shanghai, Suzhou, Hangzhou, and Nanjing, is one of the regions with the most complex photochemical processes and increasing O<sub>3</sub> pollution (Ding, Fu, Yang, Sun, Petäjä, et al., 2013). Because of the warm subtropical climate, rapid urbanization and industrialization, and intense agricultural activities as well as complex biogenic emissions (Ding, Nie, et al., 2016), the physical and chemical processes of O<sub>3</sub> formation and buildup are particularly interesting in this region (Ding, Fu, Yang, Sun, Petäjä, et al., 2013; L. Li et al., 2012; Pan et al., 2015; X. Xu et al., 2008; T. Wang et al., 2001). In the YRD, only a few studies report on the vertical O<sub>3</sub> distribution in the troposphere. Zheng et al. (2005) investigated the characteristics of vertical O<sub>3</sub> distributions below 5 km by conducting ozonesonde observations at the Lin'An regional background station. Geng et al. (2009) performed aircraft measurements of O<sub>3</sub> and several of its precursors for 3 days in autumn 2007. Very recently, there have been several studies on the vertical distribution of O<sub>3</sub> and relevant species in Shanghai based on remote sensing, tethered-balloon, and unmanned aerial vehicle (X.-B. Li et al., 2018; Xing et al., 2017). Most of these studies were conducted in the east or southeast part of the YRD region. However, in the western YRD, that is, the downwind region of the city clusters in photochemically active season, there is still a lack of investigation on the vertical profile of O<sub>3</sub>.

In this study, we conducted intensive vertical measurements of O<sub>3</sub> using instruments onboard tethered balloons, together with ground-based in situ and remote sensing measurements, at the Station for Observing Regional Processes of the Earth System (SORPES) in Nanjing, within the western YRD, for a multi-day O<sub>3</sub> episode during 11–15 June 2014. Previous studies have shown that the monthly mean O<sub>3</sub> concentration reaches its maximum in early summer (June) in this region, with typical O<sub>3</sub> concentrations as high as 30–50 parts per billion by volume (ppbv), and agricultural straw burning activities have been found to be particularly intensive in eastern China from the end of May to mid-June (Ding, Fu, Yang, Sun, Petäjä, et al., 2013; Ding, Fu, Yang, Sun, Zheng, et al., 2013; Huang et al., 2012, 2016). In June, the prevailing wind in Nanjing is usually from the northeast plains area planted with wheat and alternately from the city cluster between Nanjing and Shanghai/Hangzhou, with intense urban/industrial emissions from the southeast

(Ding, Fu, Yang, Sun, Petäjä, et al., 2013; Ding, Fu, Yang, Sun, Zheng, et al., 2013). This study aims to gain insight into the physical and chemical causes of O<sub>3</sub> pollution during this season. With the aid of numerical modeling based on the Weather Research and Forecasting model coupled with Chemistry (WRF-Chem), Lagrangian dispersion model, and Hybrid Single-Particle Lagrangian Integrated Trajectory (HYSPLIT), we investigate the detailed processes responsible for this multiday O<sub>3</sub> episode and discuss the potential implications for air pollution control in eastern China.

## 2. Field Study and Modeling Methods

### 2.1. Description of Field Measurements and Data

The field campaign was conducted at the SORPES station at the Xianlin Campus of Nanjing University. This station is a regional *background* site generally upwind of downtown Nanjing and downwind of the YRD city cluster (Ding, Fu, Yang, Sun, Petäjä, et al., 2013; Ding, Nie, et al., 2016). O<sub>3</sub> was measured continuously using Thermo-Fisher Scientific TEI 49i. Water soluble aerosol ions (NO<sub>3</sub><sup>-</sup>, SO<sub>4</sub><sup>2-</sup>, NH<sub>4</sub><sup>+</sup>, Na<sup>+</sup>, K<sup>+</sup>, Cl<sup>-</sup>, Ca<sup>2+</sup>, Mg<sup>2+</sup>, etc.) were measured by a Monitor for Aerosols and Gases in ambient Air (designed and manufactured by Applikon Analytical B.V., the Netherlands) with a PM<sub>2.5</sub> cyclone inlet. The time resolution was 1 hr, and the instrument was calibrated on an hourly basis using a liquid internal standard (bromide lithium) to ensure a stable and reliable ion chromatograph. Concentrations of all aerosol ions and gases had a precision of 0.001 μg/m<sup>3</sup> (Xie et al., 2015). NO<sub>2</sub> was measured continuously using a Thermo-Fisher Scientific TEI 42i coupled with a highly selective photolytic converter to measure NO<sub>2</sub>. The analyzer had a detection limit of 50 parts per trillion by volume for an integration time of 5 min, with a 2-s precision of 4% and an uncertainty of 10%. (Z. Xu et al., 2013; Z. N. Xu et al., 2017). A Mini Micro Pulse LiDAR instrument (Sigma Space, Lanham, MD, USA) was used to retrieve the normalized relative backscatter profile (Spinhirne, 1993). The raw binary data files were first interpolated according to the operation manual and then processed according to Campbell et al. (2002). The correction factor for dead time was specified by the manufacturer 16 months prior to our measurement. Background noise was detected automatically in each scan and subtracted from the raw signal accordingly. The afterpulse calibrations were carried frequently during the whole measurement, and an averaged afterpulse *profile* was used in data processing. Overlap calibration was carried out for the whole system (including the additional opal glass on the roof) by laying the whole system out horizontally during a sunny afternoon with moderate aerosol loading shortly after the campaign. The data used here were taken every 10 min on average with a vertical resolution of 15 m. Solar radiation was measured by a CNR4 net radiation sensor (KIPP & ZONEN), which was installed on a meteorological tower at the station. Detailed descriptions of the ground-based measurements of other trace gases, aerosols, and meteorological parameters were given in Ding, Nie, et al. (2016).

A portable O<sub>3</sub> monitor (Personal Ozone Monitor Model, POM, 2B Technologies, Inc.) on board a tethered balloon was used to measure vertical distributions of O<sub>3</sub>. The POM was designed to measure O<sub>3</sub> in air over a wide dynamic range extending from a lower detection limit of 4 ppbv to an upper limit of 10 parts per million based on the technique of absorption of ultraviolet light at 254 nm. The POM was fixed approximately 2 m beneath the balloon. The measurement interval was set to 10 s, and the data were averaged to 1 min in the analysis here. The POM data were compared with TEI 49i data before and after the campaign. The comparison shown in the supporting information Figure S1 suggests that the two instruments agreed very well with each other ( $R > 0.99$ , with a slope of 0.94). Because the TEI 49i was routinely calibrated for long-term measurement at the SORPES station, the POM data used here were corrected with this calibration curve. A total of 23 O<sub>3</sub> vertical profiles was taken during the 4-day campaign. The time interval between profiles was approximately 3 hr, including 1–1.5 hr for the ascent and descent of the balloon and the remainder for data transfer and battery charging. The top height of profiles ranged from 1 to 2 km, dependent on the upper-level wind conditions. The maximum height reached up to 2.15 km under a calm condition on the night of 13 June 2014. All profiles are displayed in Figure S2.

Vertical profiles from the In-service Aircraft for a Global Observing System (IAGOS) data set were also used in this study. The suite of instruments on board IAGOS aircrafts measured O<sub>3</sub>, water vapor, and carbon monoxide (CO). O<sub>3</sub> and CO measurements were based on ultraviolet absorption and infrared absorption methods, with time resolutions of 4 and 15 s, respectively. The precisions for O<sub>3</sub> and CO measurement were 2 and 5 ppbv, respectively.

**Table 1**  
*WRF-Chem Configuration Options and Settings*

Setting values	
Model domain	160 × 180
Horizontal grid	20 km × 20 km
Grid spacing	27
Vertical layers	Lambert conformal conic
Projection	
Configuration options	
Parameterization on physical/chemical processes	
Longwave radiation	RRTMG
Shortwave radiation	RRTMG
Land surface	Noah
Boundary layer	Yonsei University
Microphysics	Lin et al.
Gas Chemistry	CBMZ

*Note.* CBMZ = Carbon-Bond Mechanism version Z; RRTMG = Rapid Radiative Transfer Model for GCMs.

## 2.2. LPDM and WRF-Chem Modeling

To better understand the physical and chemical processes driving the multiday O<sub>3</sub> episode, we applied Lagrangian particle dispersion modeling (LPDM) to investigate the transport and dispersion of air masses for the observations and then conducted numerical modeling of three-dimensional Eulerian chemical transport modeling with WRF-Chem to gain a better quantitative understanding of the transport processes involved.

The LPDM was used to study the transport pathways and trace the potential sources of air masses during the campaign using HYSPLIT (Stein et al., 2015), following the method developed by Ding, Wang, and Fu (2013). Briefly, for each hour during the study period, the model was run several days backwardly with 3,000 particles released every hour at a specific height over the site. The model calculated the particle position with mean wind and turbulent transport after being released from the receptor point. The residence time of particles below the 100-m level was used to identify the *footprint* retroplume. The spatiotemporal distributions of these parti-

cles were used to identify potential source regions and their relative contribution to the air masses measured at the SORPES station. The Moderate Resolution Imaging Spectroradiometer Thermal Anomalies/Fire Daily L3 Global Product (MOD/MYD14A1), which defined fire events by calculating the brightness temperature difference among neighboring pixels, was used together with LPDM simulation results to identify agricultural straw burning locations and to estimate the potential O<sub>3</sub> impact from biomass burning.

The WRF-Chem model is an online coupled chemical transport model considering multiple physical and chemical processes, including emission and deposition of pollutants, advection, diffusion, and gaseous chemical transformation (Grell et al., 2005). In this study, we used version 3.6.1 of WRF-Chem. The model was run in a domain centered at 115°E and 33°N, covering eastern China with a grid resolution of 20 km. The initial and boundary conditions of meteorological fields were constrained by National Centers for Environmental Prediction global final analysis (FNL) data with a spatial resolution of 1° × 1°. The simulations were conducted for 11–15 June 2014 with a 7-day spin-up.

We used the Lin microphysics scheme, the Rapid Radiative Transfer Model for GCMs shortwave and longwave radiation scheme, the Noah land surface scheme, and the YSU PBL scheme. The Carbon-Bond Mechanism version Z photochemical mechanism was adopted for atmospheric chemistry processes. Detailed information on the model setup is listed in Table 1. The anthropogenic emission intensities of trace gases (CO, CO<sub>2</sub>, SO<sub>2</sub>, and nitrogen oxides), ammonia (NH<sub>3</sub>), methane, and nonmethane organic compounds were estimated based on the Multiresolution Emission Inventory for China database (M. Li et al., 2017). The biogenic VOC and NO emissions were calculated online using the Model of Emissions of Gases and Aerosols from Nature embedded in WRF-Chem (Guenther et al., 2006). The Fire Inventory from the National Center for Atmospheric Research was applied as biomass burning emissions due to its high temporal and spatial resolution (Wiedinmyer et al., 2011).

To investigate the contributions of individual physical and chemical processes to variations in atmospheric O<sub>3</sub> concentrations, we performed diagnostic analysis in the WRF-Chem simulation. The change rates of chemical species concentrations due to the dynamic and chemical production/loss processes are described by a set of mass continuity equations in the model. The change in O<sub>3</sub> concentration due to vertical mixing, photochemical chemistry, and advection (including both horizontal and vertical components) was calculated and recorded at each integration step.

## 3. Field Measurement Results

### 3.1. General Characteristics and Synoptic Weather

Previous studies have shown that surface O<sub>3</sub> concentrations at Nanjing reach the maximum in June (Ding, Fu, Yang, Sun, Petäjä, et al., 2013; Tang et al., 2013). From early to middle June 2014, a multiday O<sub>3</sub> episode occurred in Nanjing. The daily maximum O<sub>3</sub> concentration at the SORPES station gradually increased from approximately 50 ppbv in 1–2 June to approximately 120 ppbv on 8–9 June and reached 141.5 and 141.7

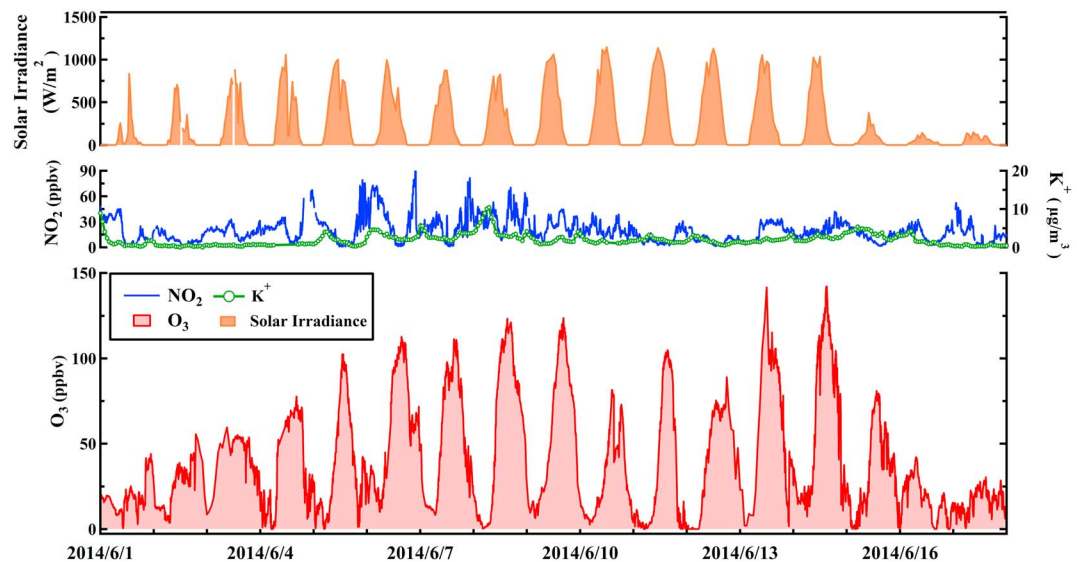


**Figure 1.** Time series of ground-based observations of  $\text{O}_3$ ,  $\text{NO}_2$ , and  $\text{K}^+$  concentrations and global solar radiation at the Station for Observing Regional Processes of the Earth System in Nanjing, China, during June 2014.

ppbv on 13 and 14 June, respectively, which were the highest and second highest hourly  $\text{O}_3$  concentrations observed at the SORPES station in 2014. Within the 2-week period, there were 8 days (5–9, 11, 13, and 14 June 2014) with hourly  $\text{O}_3$  concentrations exceeding 100 ppbv. Supported by numerical air quality forecast, our tethered-balloon measurement campaign was conducted during 11–14 June 2014, which successfully captured the highest  $\text{O}_3$  episode in 2014 and covered the evolution of photochemical pollution during this 2-week  $\text{O}_3$  episode.

Meteorological conditions, especially solar radiation, and  $\text{O}_3$  precursors were the main factors influencing  $\text{O}_3$  formation. The time series of global radiation measured at the SORPES station given in Figure 1 shows that there was generally continuous sunny weather during 4–14 June 2014, with 4–8 June influenced by clouds during the middle of the day and 9–14 June experiencing clear sky conditions. However, during 10–13 June, the  $\text{O}_3$  concentration decreased substantially, although the solar radiation reached its maximum during the 2-week period, indicating the importance of influences from other factors, such as the presence of  $\text{O}_3$  precursors and long-range transport related to the change of synoptic weather conditions (Ding, Fu, Yang, Sun, Petäjä, et al., 2013; Y. Zhang et al., 2016). Consistent with previous studies in this region (Cheng et al., 2014; Nie et al., 2015), the biomass burning tracer,  $\text{K}^+$ , showed continuously high signal during 5–16 June 2014, indicating a potential impact from intense straw burning during the wheat harvest season in this region (Ding, Fu, Yang, Sun, Petäjä, et al., 2013; Ding, Fu, Yang, Sun, Zheng, et al., 2013).  $\text{NO}_2$ , one of the  $\text{O}_3$  precursors, showed a low concentration during 11–13 June, along with a minor decrease of  $\text{K}^+$  concentration.

Figures 2a and 2b show the mean geopotential height and wind field at 500 and 850 hPa, respectively, during the measurement campaign period. Figure 2a shows a strong subtropical high located over the Pacific and a low-pressure system (cyclone) over northeast Asia at 500 hPa. Under such conditions, the YRD region was situated in front of a ridge and behind a trough, influenced by strong northwest flows. A continental high covered eastern-central China at 850 hPa (Figure 2b), and several distributed high-pressure systems could also be seen from the surface weather chart, with one covering the YRD region in eastern China (Figure 2c). As illustrated by Ding, Fu, Yang, Sun, Petäjä, et al. (2013), such large-scale stagnant weather is a typical synoptic condition corresponding with  $\text{O}_3$  pollution in eastern China. Therefore, our tethered-balloon field campaign captured the most typical weather related to  $\text{O}_3$  pollution in this region. The averaged retroplume calculated by LPDM for air masses at the SORPES station during the period (Figure 2d) showed three main transport pathways: long-range transport from the northeastern coastal China, maritime air passing through the YRD, and local air masses recirculated through the YRD.

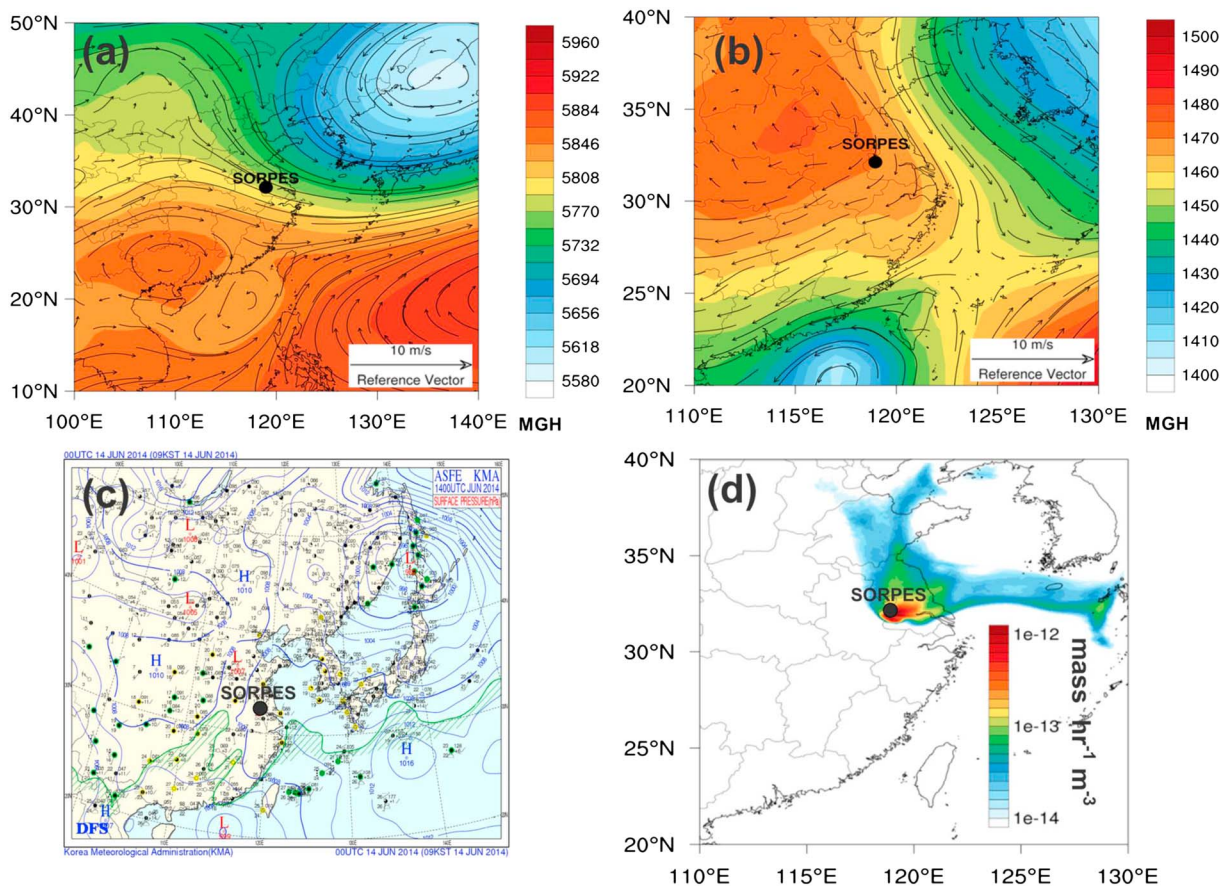


**Figure 2.** Averaged meteorological conditions at different pressure levels and air mass transport patterns during the episode. (a) Mean geopotential height (color scale) and wind field at 500 hPa, (b) mean geopotential height (color scale) and wind field at 850 hPa during 11–15 June 2014, (c) surface weather chart on 14 June 2014 (provided by the Korea Meteorological Administration), and (d) averaged 3-day retroplume (footprint of time residence) calculated from Lagrangian particle dispersion modeling during 11–15 June 2014.

### 3.2. Two Typical Cases for Biomass Burning and Residual-Layer Vertical Mixing

#### 3.2.1. Case I—Biomass Burning Plume in Lower Troposphere

Biomass burning can produce large amounts of trace gases and aerosols, which play important roles in atmospheric chemistry (Chen et al., 2017; Cheng et al., 2014; Ding, Fu, Yang, Sun, Petäjä, et al., 2013; Ding, Fu, Yang, Sun, Zheng, et al., 2013; Liu et al., 1999; Wiedinmyer et al., 2011; Zhou et al., 2013). Several studies (e.g., C. Y. Chan et al., 2003; Liu et al., 1999; Zhou et al., 2013) reported substantial and regular  $\text{O}_3$  enhancement in the lower troposphere (2.0–4.5 km) in south China during spring and attributed its main cause to biomass burning in Southeast Asia. In eastern China, studies showed that agricultural straw burning during the harvest seasons of wheat (from the end of May to middle June) contributed to a huge amount of aerosol emissions and  $\text{O}_3$  pollution. Over  $10 \text{ kg}\cdot\text{km}^{-2}\cdot\text{day}^{-1}$  black carbon and primary trace gases were emitted during one severe straw burning episode (Huang et al., 2012). Episodes reported at SORPES show that  $\text{O}_3$  could increase to over 120 ppbv accompanied by  $\text{PM}_{2.5}$  concentrations reaching  $350 \mu\text{g}/\text{m}^3$  as a result of biomass burning (Chen et al., 2017; Ding, Fu, Yang, Sun, Zheng, et al., 2013; Huang et al., 2016).

During 11–12 June 2014, lidar measurements showed a layer of high aerosol backscatter located in the free troposphere, with a height of approximately 3 km on the morning of 11 June, which gradually decreased to less than 2 km on the morning of 12 June (Figure 3a). To capture this episode, tethered-balloon measurements were conducted at 11:00 local time (LT) on 11 June. Interestingly, the IAGOS program (Petzold et al., 2012, 2015) also had obtained measurements of the event from onboard a Lufthansa international flight between Nanjing and Frankfurt on 11 June. IAGOS provided two vertical profiles of both  $\text{O}_3$  and CO during the descent and ascent of the airplane over the Nanjing International Airport, which was approximately

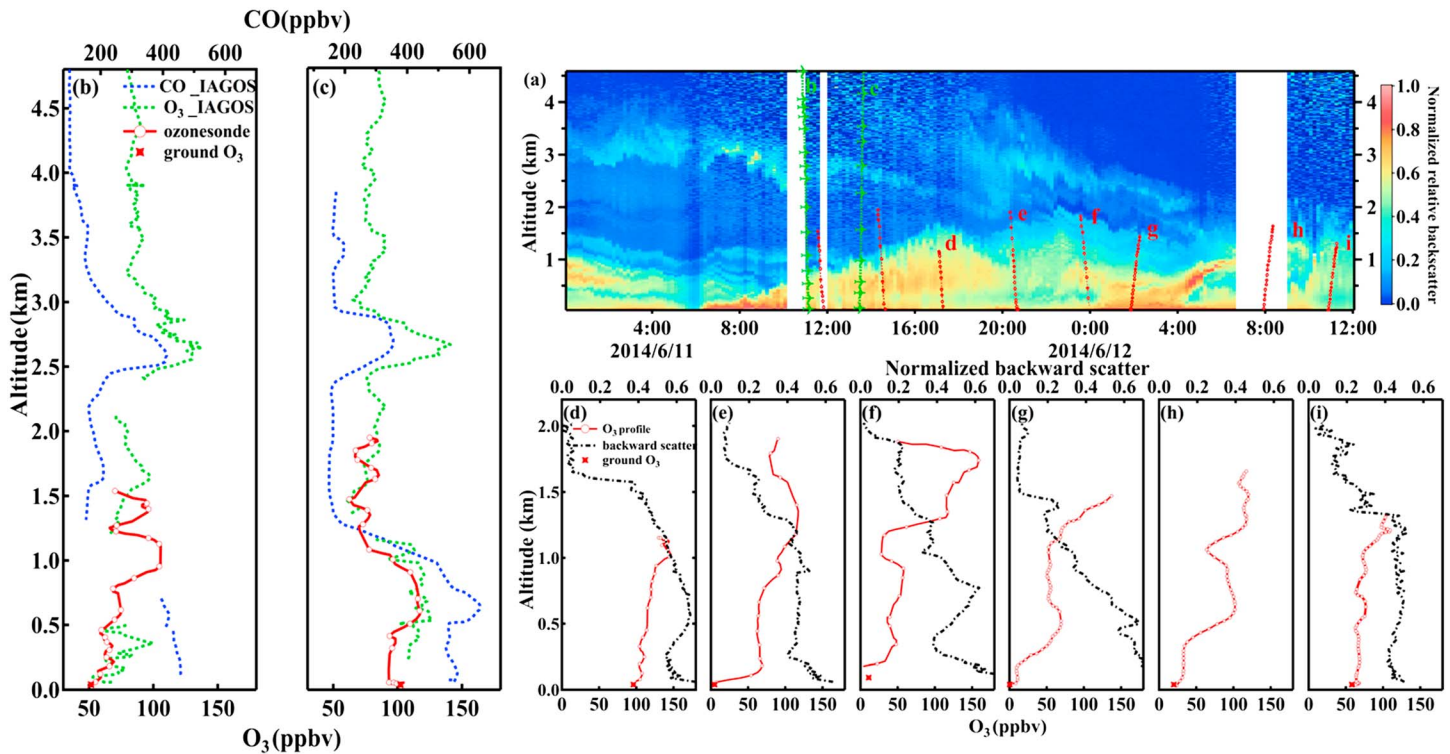


**Figure 3.** (a) Vertical cross section of lidar-measured normalized aerosol backscatter as a function of time during 11–12 June 2014, marked with the tracks of aircraft (green dotted lines with plane markers) and tethered-balloon measurements (red dotted lines). Airborne measurement of O<sub>3</sub> and CO concentration over the Nanjing International Airport by the IAGOS aircraft around (b) 11:00 LT and (c) 13:30 LT, respectively, and tethered-balloon measurement of O<sub>3</sub> at the SORPES station at approximately 12:00 and 14:45 LT, 11 June 2014. (d–i) Vertical profiles of O<sub>3</sub> (red line marked with circles), normalized aerosol backscatter (black dashed curve), and ground-based O<sub>3</sub> concentrations at SORPES (red stars) at approximately 17:00 and 20:30 LT on 11 June and 00:00, 02:00, 08:00, and 11:00 on 12 June 2014, respectively. Note that the track of profiles shown in Figures 3b–3i are given in Figure 3a. SORPES = Station for Observing Regional Processes of the Earth System; IAGOS = In-service Aircraft for a Global Observing System.

40 km south of the SORPES station. The timing of the aircraft profiles was quite close to our two tethered-balloon studies. Figures 3b and 3c show the profiles measured by both the IAGOS aircraft over the airport and the tethered balloon over the SORPES station. The O<sub>3</sub> profiles measured by the two platforms matched well with each other below 1.5 km, especially with respect to the altitude of O<sub>3</sub> in the PBL, which was close to 1.2 km at approximately 14:00 LT, as shown by the lidar-measured aerosol backscatter. With tethered balloon and aircraft, Mazuca et al. (2017) also reported a good agreement of O<sub>3</sub> observations within the PBL in Houston.

The IAGOS profiles showed a peak of both O<sub>3</sub> and CO at the altitude of 2.5 to 3.0 km, with maximum concentrations of approximately 130 and 400 ppbv, respectively, corresponding to a layer of aerosol backscatter enhancement. The positive correlation between O<sub>3</sub>, CO, and aerosols indicated that the air masses were photochemically aged plumes. To identify the source of this plume, a 7-day backward LPDM simulation was conducted at an altitude of 2.6 km above ground level. Figure 4 shows the averaged retroplume for this plume on the Moderate Resolution Imaging Spectroradiometer fire detection map (from MOD14A1 during the 7-day backward time period). This confirmed that the transport pathway of the O<sub>3</sub> plumes measured by the IAGOS aircraft in the free troposphere was associated with a long air mass residence time over the straw burning areas north of Jiangsu province and south of the adjacent Shandong province. Aerosol backscatter profiles retrieved from the CALIPSO satellite also showed enhancement of smoke aerosols centered at 116.5°E, 32.9°N at a height of 2.5–5.5 km, during this period (Figure S3).

The lidar-measured backscatter profiles at the SORPES station showed a continuous downward transport of this plume from 11 to 12 June and mixing with the daytime PBL on 12 June (Figure 3a). Figures 3d–3i show the O<sub>3</sub> profiles measured by the tethered balloon and the corresponding lidar aerosol backscatter profiles for each sounding profile. Clear stratification of O<sub>3</sub> and aerosols appeared on the night of 11 June. For example,

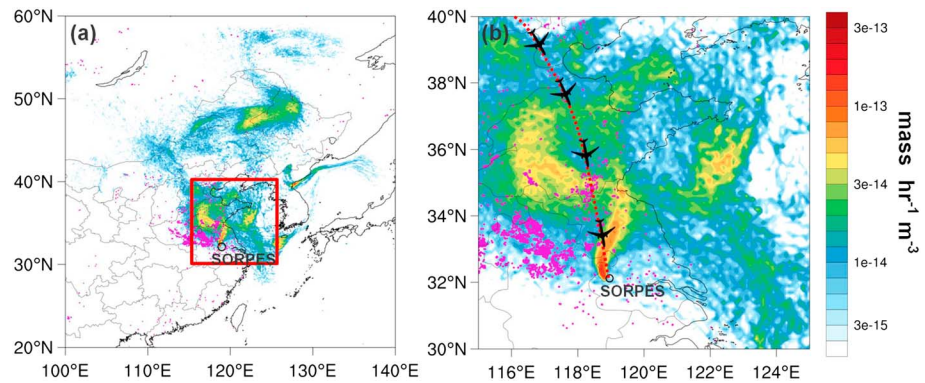


**Figure 4.** Averaged 7-day surface retroplume (color coded) calculated from Lagrangian particle dispersion modeling simulations for a receptor at an altitude of 2.6 km above the SORPES station on 11 June and the satellite-retrieved fire count data (pink points) during the 7-day period before the event in (a) eastern Asia and (b) a zoomed region on the eastern coast of China, marked as red box in Figure 4a. Note that the In-service Aircraft for a Global Observing System flight track is marked in Figure 4b. SORPES = Station for Observing Regional Processes of the Earth System.

well-mixed  $O_3$  existed below the altitude of 1 km, but an enhancement of  $O_3$  with a maximum over 150 ppbv appeared between 1.3 and 1.8 km above the PBL during 23:00 LT 11 June to 3:00 LT 12 June (Figures 3f and 3g), which corresponded to the same biomass burning plume layer identified by the IAGOS aircraft. Around noon of 12 June, the  $O_3$  and aerosol backscatter profiles did not show such a stratified structure but a more unified vertical distribution because of the strong mixing in the daytime convective PBL.

To further understand the potential source regions of upper-PBL air masses during different times within this episode, 3-day backward LPDM simulations were conducted at an altitude of 1.5 km over the SORPES station for three different time periods: 17:00–21:00 LT 11 June, 23:00 LT 11 June to 03:00 LT 12 June, and 05:00–09:00 LT 12 June. Figures 5a–5c show the averaged retroplumes for the three periods. During the first and third periods, air masses showed more influence from Nanjing and the nearby northeastern region in the Jiangsu province (Figures 5a and 5c), but during the second period, the air masses approximately 1.5 km had the longest resident time over biomass burning areas in the north of Jiangsu province and to the south of Shandong province (Figure 5b). The potential source region given in Figure 5b was quite similar to that of the IAGOS airplane-observed biomass burning plumes around noontime of 11 June (Figure 4b). These results confirmed that the tethered-balloon measurement during the night of 11 June captured the same biomass burning plume belt measured by the IAGOS aircraft 12 hr earlier.

Because the fixed station conducts measurements from an Eulerian perspective, the changes in plume altitude with time reflected a spatial distribution along the wind-facing direction, that is, from south to north

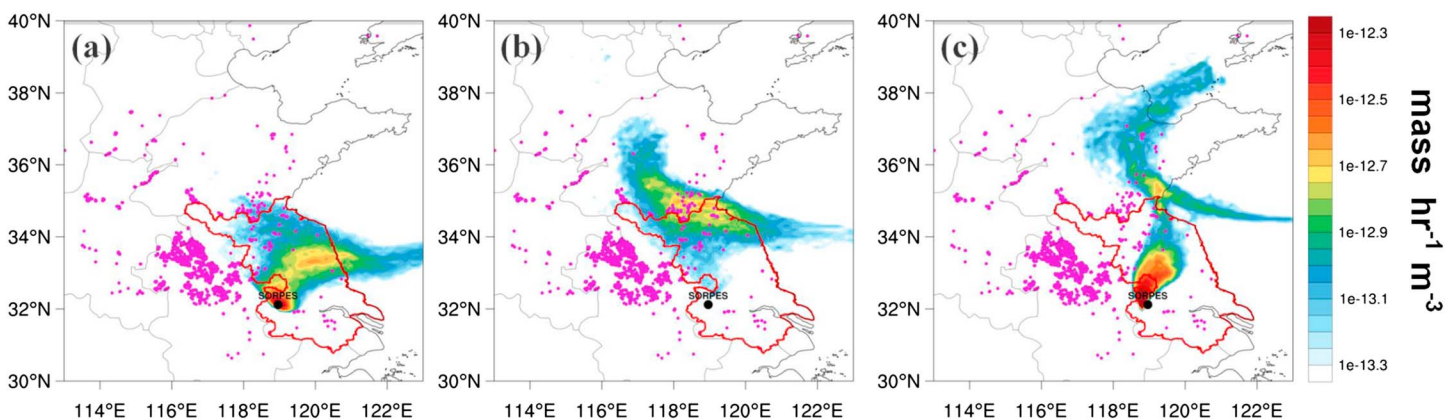


**Figure 5.** Same as Figure 4b but showing 3-day backward retroplumes calculated for receptors at the altitude of 1,500 m above the Station for Observing Regional Processes of the Earth System during (a) 17:00–21:00 LT 11 June, (b) 23:00 LT 11 June to 03:00 LT 12 June, and (c) 05:00–09:00 LT 12 June 2014. Note that the fire count data here are also averaged for a 3-day period before the event. Jiangsu province is outlined with a red line.



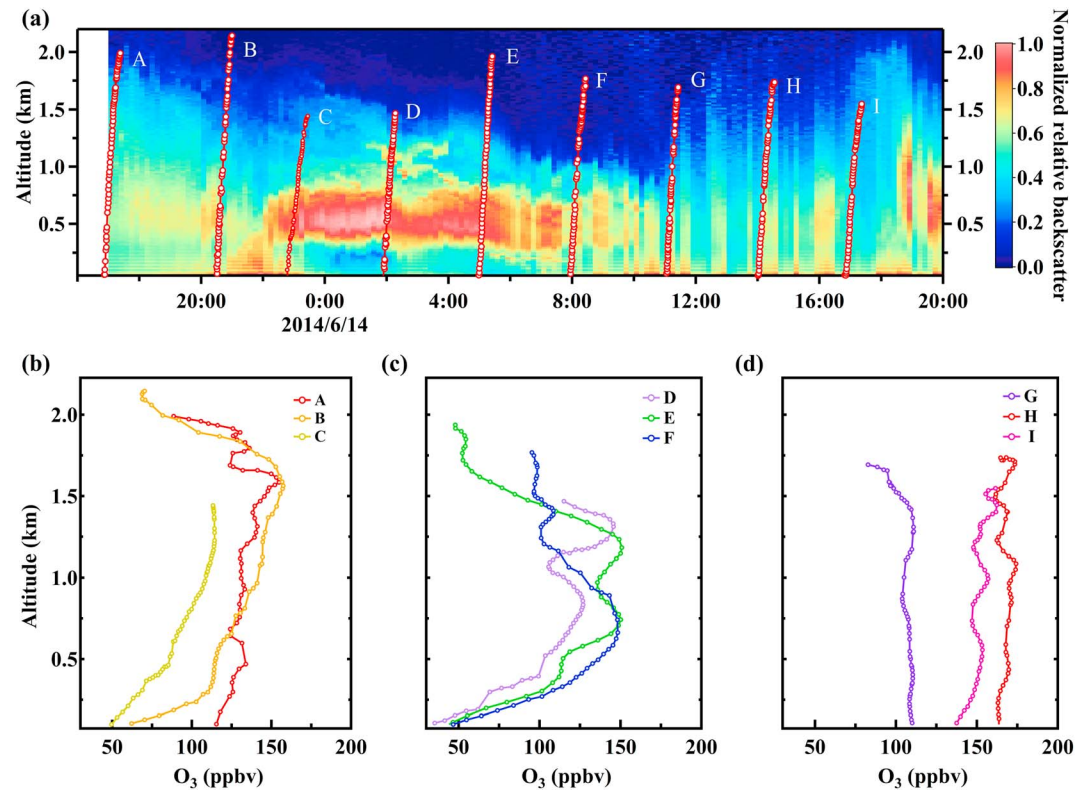


**Figure 6.** (a) Vertical cross section of lidar-measured normalized aerosol backscatter as a function of time during 13–14 June 2014, marked with the tracks of tethered-balloon measurements. (b–d) Vertical profiles of O<sub>3</sub> from tethered-balloon measurements over the Station for Observing Regional Processes of the Earth System during 17:00–23:00 LT 13 June, 02:00–08:00 LT 14 June, and 11:00–17:00 LT 14 June 2014, respectively. Note that the tracks of these balloon profiles are given in Figure 6a.

(Figure 2b). Because the high-pressure system, that is, anticyclone, forced more subsidence of air in its core, the spatial characteristics of anticyclone, as shown in Figure 2b, favored a south high/north low structure of biomass burning plumes and a southerly transport pathway. The results demonstrated that with different measurement platforms, for example, airplane, tethered balloon and lidar, a three-dimensional structure and the evolution of O<sub>3</sub> pollution episode could be well captured.

### 3.2.2. Case II—Vertical Mixing of Photochemically Aged Air From the Residual Layer

Previous studies using LPDM (e.g., Ding, Fu, Yang, Sun, Petäjä, et al., 2013) demonstrated that summertime O<sub>3</sub> episodes at the SORPES station were mainly influenced by urban plumes from city clusters along the Nanjing-Shanghai axis. However, the detailed mechanisms and key processes of subregional transport within the PBL are still unclear. During the night of 13 June to 14 June, the tethered-balloon and lidar measurements captured the vertical mixing of residual-layer preexisting aged subregional plumes.

Figure 6 shows the Micro Pulse LiDAR-measured aerosol backscatter and tethered-balloon-measured O<sub>3</sub> vertical profiles. A well-defined three-layer stratified structure could be identified in the lidar aerosol profile from 22:00 LT 13 June to approximately 08:00 LT 14 June 2014 (Figure 6a). The layer with the highest aerosol backscatter existed between the altitudes of 400 and 900 m. Below the aerosol layer, the backscatter was low with a unified vertical structure, and above that high aerosol layer, a moderate backscatter with some narrow multilayer plumes could also be observed between 900 and 1,500 m (Figure 6a). The multilayer aerosol structure demonstrated the evolution of the PBL in the city cluster region. The air temperature profiles shown in Figure 7 clearly demonstrated that in the early morning of 14 June, there was an inversion layer of air temperature near the ground surface, indicating that the high aerosol layer in the upper level was an aged residual-layer plume. The aerosol plume in the residual layer corresponded to an air temperature increase, which could be explained by the heating effect due to light-absorbing aerosol, like black carbon, from the city cluster (Ding, Huang, et al., 2016; Huang et al., 2018; Z. Wang et al., 2018). After sunrise, as

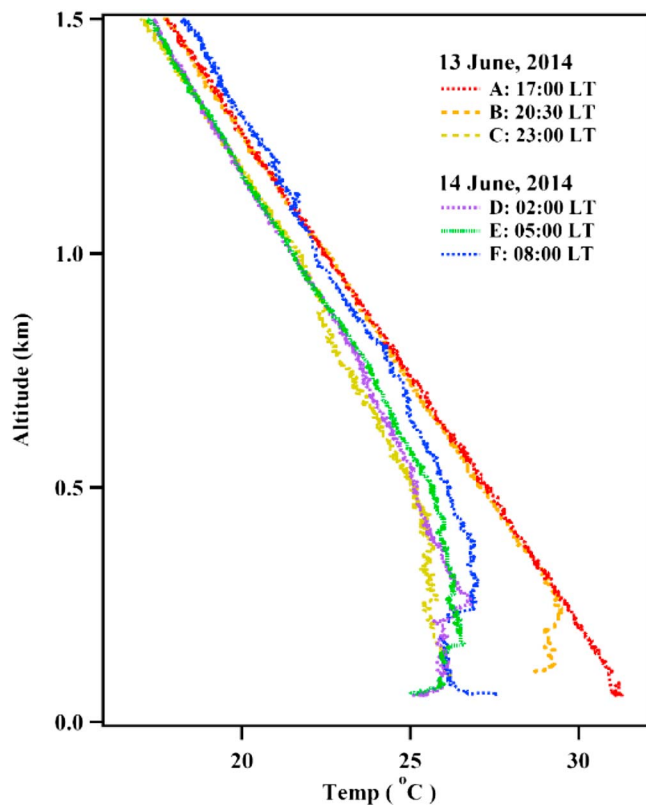


**Figure 7.** Vertical profiles of air temperature measured during 13–14 June 2014.

solar radiation heating the ground surface, the PBL started to develop with increasing convective motion, thereby promoting the vertical mixing of pollutants. Accordingly, the stable stratification with multilayer pollutants was broken. The backscatter profiles also showed that such stratification was disturbed in the late morning with the plume descending to the ground and being further vertically dispersed as the PBL developed, resulting in a unified aerosol vertical distribution in the afternoon. Such a phenomenon demonstrated the classical diurnal variation of the PBL structure (e.g., Stull, 1988).

Figures 6b–6d represent the  $O_3$  profiles from the tethered balloon during 13–14 June 2014, showing three different stages of PBL  $O_3$  profiles during this episode. In the late afternoon of 13 June, the  $O_3$  profiles showed an overall daytime buildup of high  $O_3$  concentration within the entire PBL below the altitude of 2 km. During the nighttime, the surface and lower PBL  $O_3$  concentration decreased gradually. The chemical loss through the titration of NO and dry deposition were the main causes for the decrease in nighttime  $O_3$  concentrations (Ding et al., 2008; Schnell et al., 2016). Based on diurnal variation analysis of PBL  $O_3$  with the long-term aircraft measurements from the MOZAIC program, Ding et al. (2008) also reported such a phenomenon in Beijing. During the second stage, the surface inversion of air temperature was well established (Figure 7), and the deposition and NO titration only influenced the  $O_3$  concentration within the nocturnal PBL below the altitude of approximately 400 m. The aged plume in the residual layer remained at a high concentration (Ding et al., 2008; Neu et al., 1994; J. Zhang & Rao, 1999). However, the residual-layer  $O_3$  profiles also showed a two-layer structure, with one layer corresponding to the high aerosol layer shown by lidar measurement (Figure 6a) and the other with even higher  $O_3$  concentrations above the

aerosol layers. The different  $O_3$ /aerosol ratios in the two layers suggested different sources or different photochemical ages of the air masses. Based on continuous measurement at the SORPES station, Ding, Fu, Yang, Sun, Petäjä, et al. (2013) reported a positive correlation between  $PM_{2.5}$  and  $O_3$  in summer, which were usually from the main source region in the YRD city cluster. The third stage experienced the development of the daytime PBL structure. During this stage,  $O_3$  showed a unified concentration within the PBL after the residual-layer aged plumes were vertically mixed. Then, the unified  $O_3$  vertical profiles showed a concurrent increase and daytime buildup within the entire PBL. Ding et al. (2008) also demonstrated this phenomenon in Beijing based on climatological data from the MOZAIC program.

To investigate the potential source region of this case, Figure 8 shows a 3-day backward retroplume calculated by LPDM for different altitudes (100, 600, and 1,500 m) in the early morning (00:00–04:00 LT) and afternoon (12:00–16:00 LT) of 14 June. During 00:00–04:00 LT, the retroplumes at the three altitudes showed distinctly different source regions: fast transport from the north edge of the YRD cities in the lower PBL (Figure 8c), a significant influence from the YRD cities to the east (Changzhou, Wuxi, Nantong, etc.) in the residual layer (600 m; Figure 8b), and more regional influences at the altitude of 1,500 m with potential biomass burning sources from north Jiangsu and south Shandong province mixed with urban plumes in the YRD region (Figure 8a). In the afternoon, the retroplumes at different altitudes showed identical patterns, with a source region mainly from the YRD city clusters (Figures 8d–8f). The similarity in the transport patterns was consistent with the unified vertical profile of aerosol backscatter and  $O_3$ , indicating an influence from the strong vertical mixing from daytime convection in the PBL.

This case demonstrates how the vertical mixing of photochemically aged urban plumes in the residual layer influences the diurnal cycle of  $O_3$  and contributes to the daytime  $O_3$  buildup downwind of the YRD city clusters. A similar case was reported in North America from aircraft measurements (J. Zhang & Rao, 1999). Here our tethered-balloon measurements provided a clearer picture of the regional transport coupled with PBL processes in the formation of photochemical pollution in the western YRD during summer (Ding, Fu,

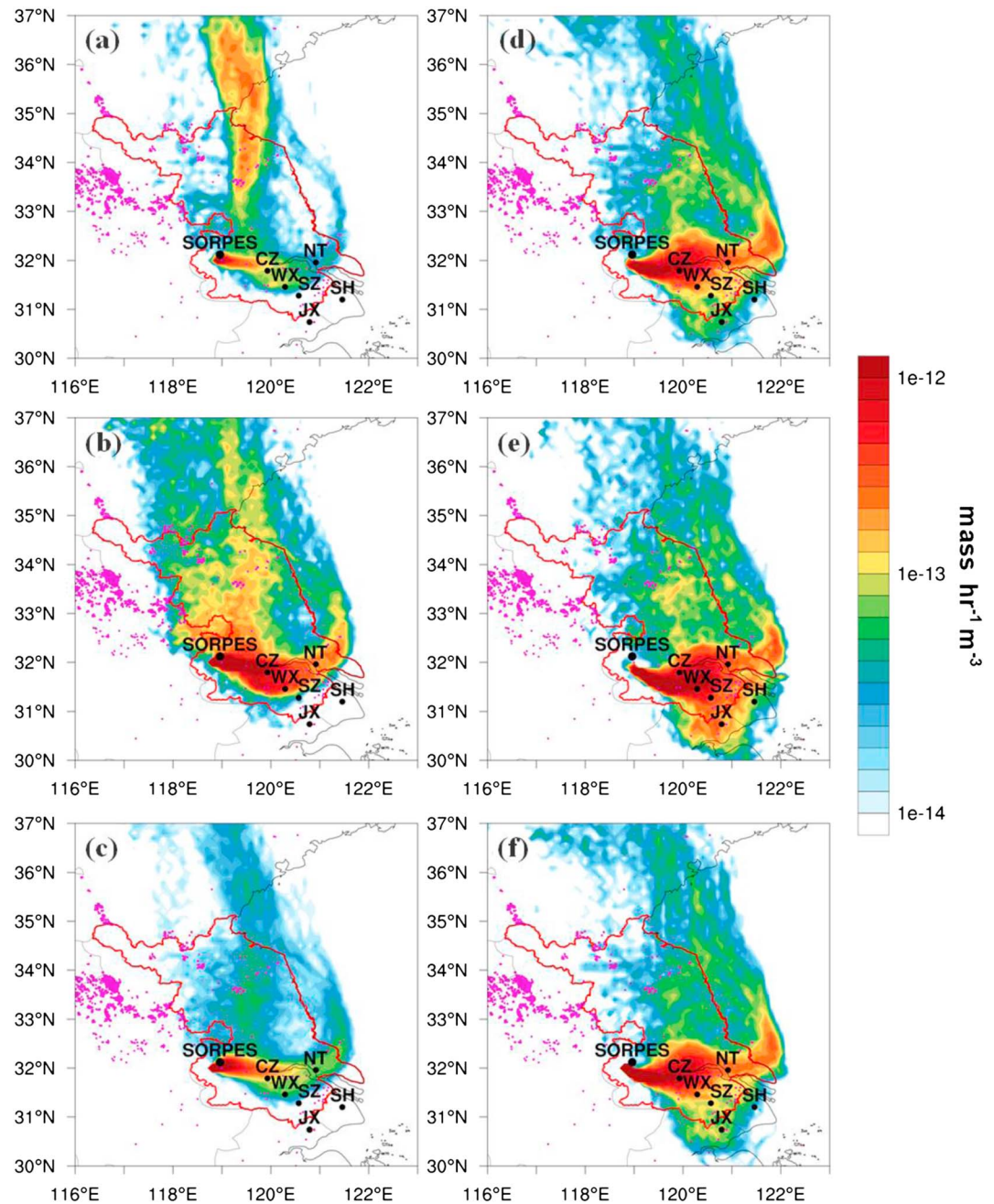


**Figure 8.** Averaged retroplumes calculated from 3-day backward Lagrangian particle dispersion modeling simulations for receptors at different altitudes (1,500, 600, and 100 m, respectively) over the SORPES station during (a–c) 00:00–04:00 LT 14 June and (d–f) 12:00–16:00 LT 14 June. Jiangsu province is outlined with a red line. The main cities in the Yangtze River Delta region are marked on the map. SH = Shanghai; JX = Jiaying; SZ = Suzhou; WX = Wuxi; NT = Nantong; CZ = Changzhou. Fire counts averaged for the 3 days before the events are also given in Figure 8. SORPES = Station for Observing Regional Processes of the Earth System.

Yang, Sun, Petäjä, et al., 2013). As mentioned above, 14 June had the highest hourly  $O_3$  record observed at the SORPES station in 2014. For that day, the surface  $O_3$  concentration also showed a dramatic increase in the early morning, which could easily be misinterpreted as a fast in situ photochemical production. The intensive vertical measurements clearly demonstrate the influence of vertical mixing from residual-layer aged plumes in enhancing the early morning  $O_3$  at the ground surface, and the daytime  $O_3$  buildup after the regional aged plume was well mixed with local emission within the entire PBL.

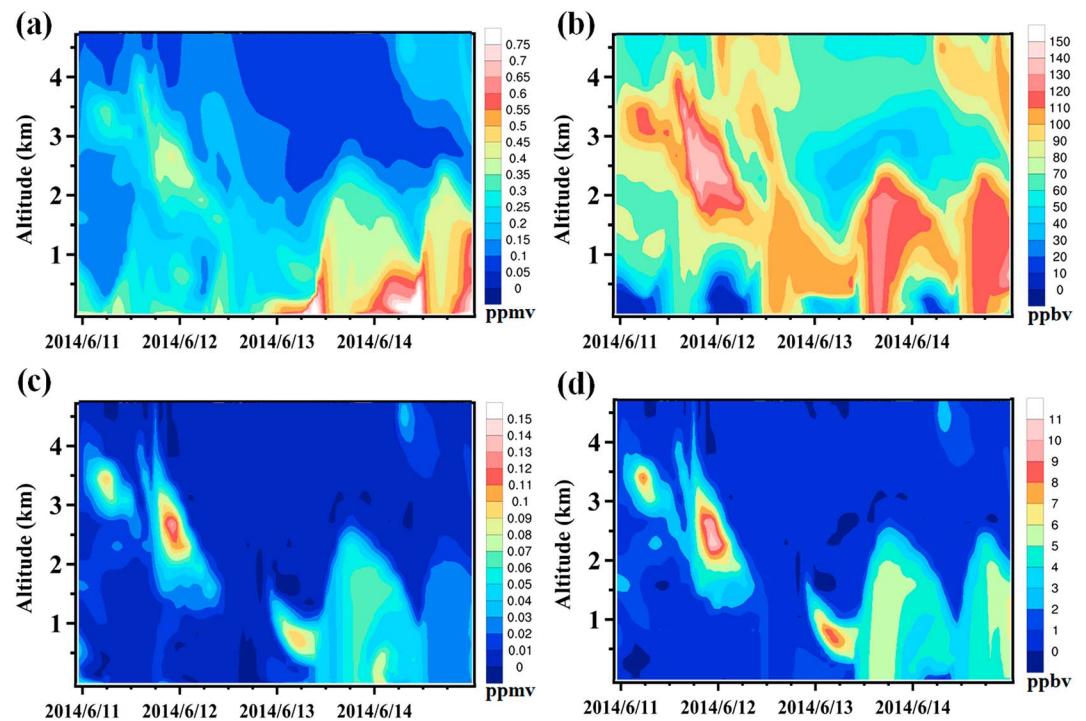


**Figure 9.** Vertical cross section of WRF-Chem simulated (a) CO and (b) O<sub>3</sub> over the Station for Observing Regional Processes of the Earth System as a function of time during 11–14 June 2014, and the impact of biomass burning on the vertical cross section of (c) CO and (d) O<sub>3</sub>, corresponding to Figures 9a and 9b, calculated from the parallel WRF-Chem simulations with/without biomass burning emission considered. WRF-Chem = Weather Research and Forecasting model coupled with Chemistry.

#### 4. Numerical Modeling With WRF-Chem

To gain a more quantitative understanding of different sources and processes driving the two O<sub>3</sub> episodes, we conducted WRF-Chem simulations for the period of 11–15 June 2014. To differentiate the contributions from biomass burning and fossil combustion sources, we performed two parallel runs with one including all emissions and the other excluding biomass burning emissions. The difference between the two runs was used to determine the contribution from biomass burning emission. The simulation that included all the emissions was used for model validation and further diagnostic analysis.

##### 4.1. Ozone Enhancement by Biomass Burning

Comparisons with available meteorological and chemical measurements validate that the WRF-Chem simulation was capable of reproducing this pollution episode (Figures S5–S7). Figure 9 shows the vertical cross section of CO and O<sub>3</sub> over the SORPES station as a function of time during 11–14 June. A comparison of the vertical cross sections of CO (Figure 9a) and aerosol backscatter (Figure S2) showed that the WRF-Chem simulations captured the vertical distribution and evolution of air pollutants in the lower troposphere during this multiday O<sub>3</sub> episode well. It showed an overall descent of plumes from an altitude of approximately 3 km on 11 June to the upper PBL on 12 June, the higher PBL on 13 June, and the enhanced residual-layer pollution in the early morning of 14 June (Figure 9a). For O<sub>3</sub>, the modeling results gave a similar pattern with CO and showed good agreement with respect to quantity with the ground-based and tethered-balloon measurements, such as the highest daytime O<sub>3</sub> on 13 and 14 June, the gradually decreased trend of daytime O<sub>3</sub>, and titration of O<sub>3</sub> in the nocturnal PBL during the nighttime of these days (Figure 9b).

Based on the simulation results of the two parallel runs, Figures 9c and 9d show the contribution of biomass burning to CO and O<sub>3</sub> concentrations over the SORPES station, corresponding to Figures 9a and 9b. The WRF-Chem model successfully simulated the altitude and overall structure of biomass burning plumes.

However, compared with the IAGOS aircraft measurement, which showed an increase of CO and O<sub>3</sub> of approximately 200 and 50 ppbv, respectively, at approximately 2.5 km; the simulation results underestimated the influence of biomass burning in this case. This underestimation was probably because the emission inventory was calculated based on satellite-detected fire counts, which sometimes substantially underestimate burning due to obscuration from clouds (Hawbaker et al., 2008). There was a cloud layer above the source region of biomass burning on 10 June 2014 (Figure S3), possibly leading to underestimated fire emissions. Additionally, more smoldering fire of crop straws is associated with substantially larger emission factors of VOCs and CO than most other fuels, which tend to be underestimated in existing publications (Akagi et al., 2011). These results also showed that on 13 and 14 June, biomass burning contributed to O<sub>3</sub> concentrations in the PBL. In the early morning of 13 June, biomass burning plumes existed mainly in the residual layer, which was consistent with the lidar aerosol backscatter data shown in Figure S2. In the late afternoon of 13 June, the biomass burning plumes were well dispersed within the entire PBL, resulting in enhancement of both CO and O<sub>3</sub> concentrations.

Our tethered-balloon measurements showed that biomass burning plumes were transported downward into PBL on 12 June. To gain a clearer picture of the transport and influence of biomass burning emission, Figures 10a and 10b show the impact of O<sub>3</sub> from biomass burning, based on the two parallel simulations, in the free troposphere and at the ground surface. It is clear that a biomass burning plume belt, with a width of approximately 300 km, at an altitude of 2.5 km (Figure 10a), was transported southward. According to the emission inventory estimation of WRF-Chem based on satellite retrievals and the LPDM simulation results, these biomass burning plumes were the result of agricultural straw burning in the north of Jiangsu province and south of Shangdong province. Although Nanjing was less influenced by these biomass burning plumes at the ground surface, the enhancement of O<sub>3</sub> up to 30–40 ppbv downwind of the source regions existed in the inland areas, for example, Central China, in the following half day (Figure 10b). Ding, Fu, Yang, Sun, Petäjä, et al. (2013) reported a case of intensive biomass burning event and found that the biomass burning emission from the same regions caused O<sub>3</sub> episodes with maximum O<sub>3</sub> concentration about 140 ppbv in Nanjing after several days transport.

#### 4.2. Importance of Vertical Mixing on Surface Ozone

For Case II, the WRF-Chem simulations could reproduce the high concentrations of CO and O<sub>3</sub> in the residual layer, which was less influenced by biomass burning but a main influence from the YRD city plumes (Figure 9). Notably, the stratification of the nocturnal boundary layer was not well characterized by the WRF simulation, probably due to a relatively coarse emission inventory and vertical gridding as well as the uncertainty in parameterization of the nocturnal PBL in the model (Z. Wang et al., 2018). Figure 10c shows the spatial distribution of the WRF-Chem simulated nighttime (01:00 LT) O<sub>3</sub> concentration at an altitude of 600 m, corresponding to the location of the residual layer observed by the lidar and tethered-balloon measurements. As shown, many regions in eastern China suffered from severe O<sub>3</sub> pollution, with a concentration over 100 ppbv even at night. The highest O<sub>3</sub> concentration in the North China Plain seemed to be contributed by biomass burning and long-range transport from the YRD and Central China regions. In the YRD region, although the averaged O<sub>3</sub> concentration was not as high as that in the North China Plain, a zonal distribution of enhanced O<sub>3</sub> plumes (over 100 ppbv) along the city cluster could be clearly discerned in Figure 10c. To investigate the role of vertical mixing of residual-layer aged plume on surface O<sub>3</sub> concentration, we applied a process analysis similar to Jiang et al. (2010) and Zhu et al. (2015) to calculate the surface O<sub>3</sub> enhancement induced by vertical mixing at 09:00 LT, when the daytime convective PBL started to develop (Figure 10d). It was clearly demonstrated that on the morning of 14 June, the YRD city cluster, along the Nanjing to Shanghai axis, was substantially influenced by the vertical mixing of residual-layer aged plumes, leading to an increase rate of approximately 30 ppbv/hr in surface O<sub>3</sub> concentration at the SORPES station and even higher concentrations downwind of Shanghai.

To compare the impacts of different processes on O<sub>3</sub> vertical profiles, Figure 11 shows the time series of relative contributions from chemical, vertical mixing, and advection transport processes on the O<sub>3</sub> concentration at different altitudes (1,000 and 600 m and ground surface) over SORPES. It shows that vertical mixing was the dominant process for surface O<sub>3</sub> enhancement during the daytime, with the strongest contribution at approximately 10:00–11:00 LT (~30 ppbv/hr), corresponding to a negative contribution of vertical mixing at the altitude of 600 m (approximately –34 ppbv/hr at 10:00 LT). These results

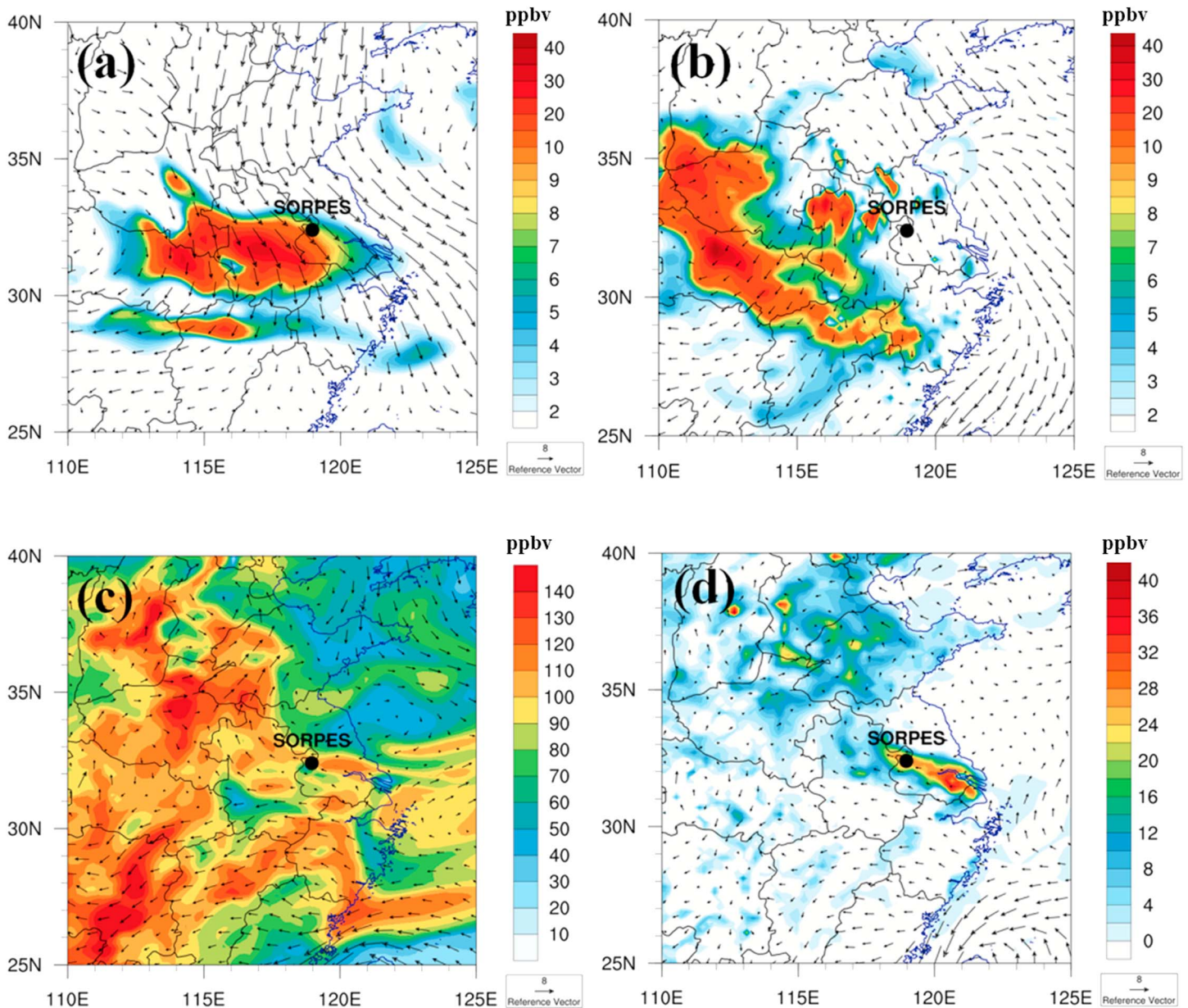


**Figure 10.** Distribution of biomass burning-induced O<sub>3</sub> enhancement for (a) the altitudes of 2.5–3 km on 00:00 LT 12 June and (b) ground surface on 14:00 LT 12 June 2014 and distributions of (c) O<sub>3</sub> at the altitude of 600 m at 00:00 LT 14 June and (d) surface O<sub>3</sub> enhancement caused by vertical mixing at 10:00 LT 14 June 2014 from Weather Research and Forecasting model coupled with Chemistry simulations with all emissions considered. SORPES = Station for Observing Regional Processes of the Earth System.

confirm that vertical mixing of aged plumes from the residual layer significantly enhanced surface O<sub>3</sub> concentrations in the morning. The contribution of vertical mixing to O<sub>3</sub> concentration showed an overall negative contribution in the middle/upper PBL, corresponding to a positive contribution at the ground surface. In contrast, the chemical production of O<sub>3</sub> was positive in the upper PBL but negative at the ground surface, except during the early morning after sunrise (07:00–09:00 LT; Figure 11c). The overall negative contribution in chemical production at the surface could be mainly caused by the titration of NO. Although the SORPES site was less influenced by local emissions, there was still NO emission in the grid that it was located in. These results suggested that regional O<sub>3</sub> transport in the upper PBL and chemical production of O<sub>3</sub> in the middle PBL and upper PBL or the residual layer at night and chemical production of O<sub>3</sub> in mixed plumes with regional and local emissions were the main

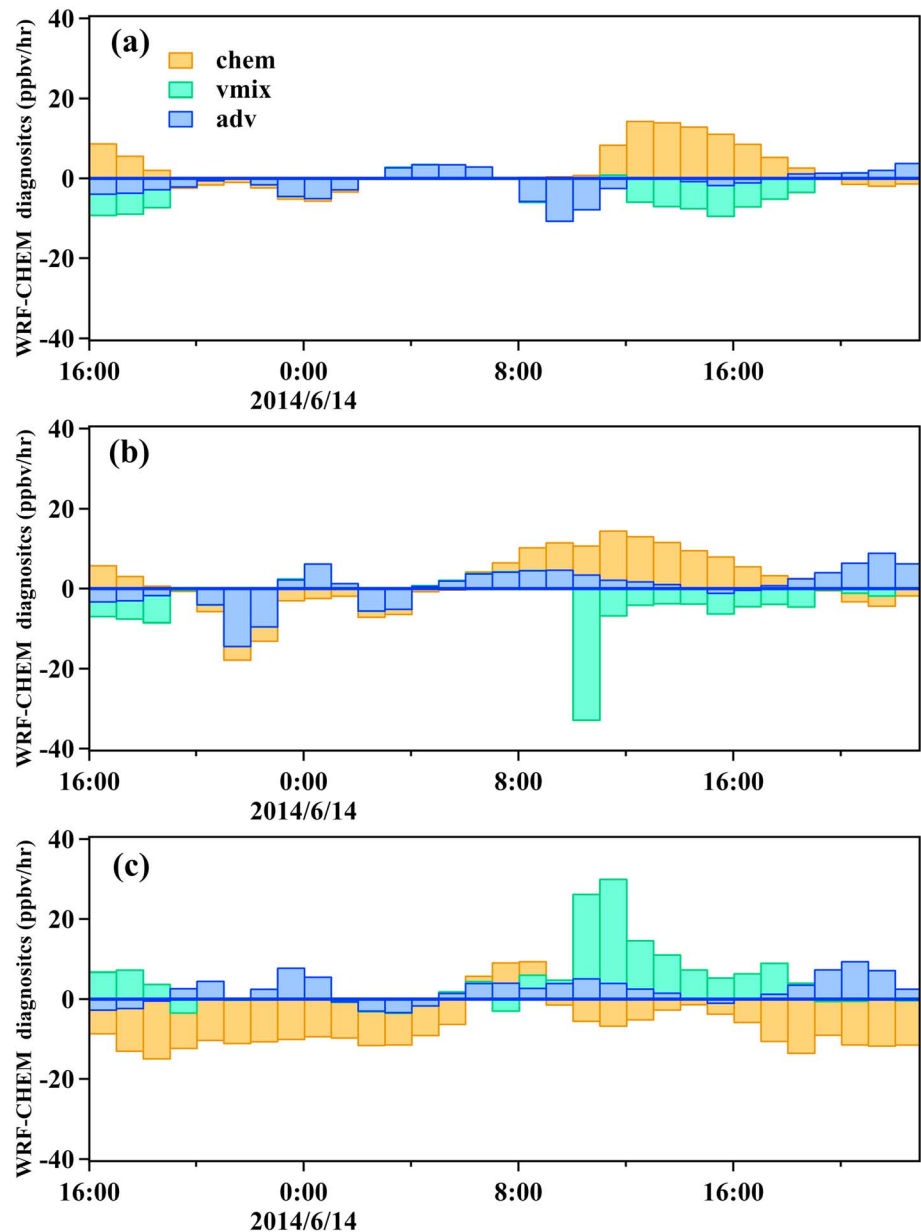


**Figure 11.** Time series of contributions of  $O_3$  from different processes (chem = chemical production; vmix = vertical mixing; adv = horizontal and vertical advection), calculated from Weather Research and Forecasting model coupled with Chemistry processes analysis, for the altitudes of (a) 1,000 m, (b) 600 m, and (c) ground surface, respectively, at the Station for Observing Regional Processes of the Earth System during 13–14 June 2014.

factors causing severe  $O_3$  pollution in this region during summer. More measurement and modeling studies are needed to investigate the detailed structure and evolution of PBL  $O_3$  downwind of the YRD city cluster in typical  $O_3$  pollution episodes under special weather conditions.

### 5. Conclusions

To understand the impact of biomass burning and city plumes on photochemical pollution in the western YRD during the early summer, we conducted an intensive tethered-balloon campaign together with ground-based in situ and remote sensing measurements at the SORPES station in Nanjing during a multiday  $O_3$  episode in mid-June 2014. Available aircraft measurements of trace gases and routine meteorological

observations were used in the data analysis. LPDM with HYSPLIT and Eulerian chemical transport modeling with WRF-Chem were used to quantify the potential source regions and contributions from different physical and chemical processes on O<sub>3</sub> pollution during this episode.

The intensive field measurement campaign captured two typical cases during the multiday O<sub>3</sub> episode. The first case was influenced by agricultural straw burning. The tethered-balloon and lidar measurements together with the IAGOS aircraft measurements consistently showed biomass burning plumes with O<sub>3</sub> enhancement of approximately 40–50 ppbv around the altitude of 3 km on 11 June 2014, and the plume descended gradually into the upper PBL over 24 hr. LPDM and satellite-retrieved fire count data showed that the plume originated from straw burning to the north of Jiangsu province and to the south of Shandong during wheat harvest season. The WRF-Chem simulations with different emission scenarios successfully captured the general pattern of biomass burning plumes at the ground surface and in the free troposphere, but the model underestimated the impact of biomass burning on O<sub>3</sub> concentration, probably because of the uncertainty in emission estimation from satellite-retrieved fire count data.

The second case was the highest hourly O<sub>3</sub> record (142 ppbv) measured at the station in 2014, a typical case showing the influence of vertical mixing of aged plumes from the residual layer on surface O<sub>3</sub> in the early morning. The residual-layer photochemically aged air, with O<sub>3</sub> concentrations up to 150 ppbv, originated from city clusters in the YRD region, especially from cities along the Nanjing-Shanghai axis. These plumes were downward transported to the ground surface during the morning as the daytime convective boundary layer developed, causing a fast increase in surface O<sub>3</sub> concentrations during the morning. The mixing of regional aged air with local emissions caused substantial photochemical production during the daytime. WRF-Chem simulations could well reproduce the vertical mixing of the aged residual-layer urban plume, and the processes analysis of WRF-Chem quantitatively showed the role of photochemical production, vertical mixing, and advection on O<sub>3</sub> concentrations at different altitudes over the SORPES station. Photochemical production contributed to the daytime O<sub>3</sub> buildup in the middle and upper PBL, while vertical mixing in the late morning caused an O<sub>3</sub> increase with a rate of approximately 30 ppbv/hr at the ground surface and a comparable negative contribution in the middle PBL.

Biomass burning and urban plumes from city clusters are the two main sources influencing O<sub>3</sub> pollution in the YRD region of eastern China. The two cases illustrated in this study demonstrate the detailed transport mechanisms of biomass burning and urban plumes to O<sub>3</sub> in downwind regions through typical synoptic and boundary layer processes. Our results highlight the importance of joint subregional air pollution control measures of different emission sources in mitigating photochemical pollution in eastern China.

#### Acknowledgments

The research was supported by the National Key Research and Development Program of China (2016YFC0200500, and 2016YFC0202000) and the National Natural Science Foundation of China (91544231, 41725020, and 91744311). The authors acknowledge the IAGOS team for conducting aircraft measurements on the Lufthansa aircraft and for providing the data and thank Prof. Yu Zhang and Dr. Lunyu Shang at Northwest Institute of Eco-Environment and Resources, Chinese Academy of Science, and Prof. Weidong Guo and Dr. Ye Liu at Nanjing University for their help with the meteorological measurements during the campaign. The numerical modeling was conducted on computing facilities at the High Performance Computing Center (HPCC) at Nanjing University. The used tethered-balloon data and surface measurements at SORPES are listed in the supporting information. IAGOS data are available at <http://iagos.sedoo.fr/>. The radiosonde observations are archived at <https://www1.ncdc.noaa.gov/pub/data/igra>, and FNL analysis data are available at <https://rda.ucar.edu/datasets/ds083.2>.

#### References

- Akagi, K., Yokelson, R. J., Wiedinmyer, C., Alvarado, M. J., Reid, J. S., Karl, T., et al. (2011). Emission factors for open and domestic biomass burning for use in atmospheric models. *Atmospheric Chemistry and Physics*, 11, 4039–4072.
- Campbell, J. R., Hlavka, D. L., Welton, E. J., Flynn, C. J., Turner, D. D., Spinhrne, J. D., et al. (2002). Full-time, eye-safe cloud and aerosol lidar observation at atmospheric radiation measurement program sites: Instruments and data processing. *Journal of Atmospheric and Oceanic Technology*, 19(4), 431–442. [https://doi.org/10.1175/1520-0426\(2002\)019<0431:FTESCA>2.0.CO;2](https://doi.org/10.1175/1520-0426(2002)019<0431:FTESCA>2.0.CO;2)
- Carter, C. A., Cui, X. M., Ding, A. J., Ghanem, D., Jiang, F., Yi, F. J., & Zhang, F. N. (2017). Stage-specific, nonlinear surface ozone damage to rice production in China. *Scientific Reports*, 7, 44,224.
- Chan, C. K., & Yao, X. (2008). Air pollution in mega cities in China. *Atmospheric Environment*, 42(1), 1–42. <https://doi.org/10.1016/j.atmosenv.2007.09.003>
- Chan, C. Y., Chan, W. L. C. L. Y., Zheng, Y. G., Cui, H., Zheng, X. D., Qin, Y., & Li, Y. S. (2003). Characteristics of a tropospheric ozone profile and implications for the origin of ozone over subtropical China in the spring of 2001. *Journal of Geophysical Research*, 108(D20), 8800. <https://doi.org/10.1029/2003JD003427>
- Chen, J., Li, C., Ristovski, Z., Milic, A., Gu, Y., Islam, M. S., et al. (2017). A review of biomass burning: Emissions and impacts on air quality, health and climate in China. *Science of the Total Environment*, 579, 1000–1034. <https://doi.org/10.1016/j.scitotenv.2016.11.025>
- Cheng, Z., Wang, S., Fu, X., Watson, J. G., Jiang, J., Fu, Q., et al. (2014). Impact of biomass burning on haze pollution in the Yangtze River delta, China: A case study in summer 2011. *Atmospheric Chemistry and Physics*, 14(9), 4573–4585. <https://doi.org/10.5194/acp-14-4573-2014>
- Cooper, O. R., Parrish, D. D., Stohl, A., Trainer, M., Nédélec, P., Thouret, V., et al. (2010). Increasing springtime ozone mixing ratios in the free troposphere over western North America. *Nature*, 463(7279), 344–348. <https://doi.org/10.1038/nature08708>
- Corsmeier, U. N., Kalthoff, O. K., Kotzian, M., & Fiedler, F. (1997). Ozone concentration jump in the stable nocturnal boundary layer during a LLJ-event. *Atmospheric Environment*, 31(13), 1977–1989. [https://doi.org/10.1016/S1352-2310\(96\)00358-5](https://doi.org/10.1016/S1352-2310(96)00358-5)
- Crawford, J., Davis, D., Chen, G., Bradshaw, J., Sandholm, S., Kondo, Y., et al. (1997). An assessment of ozone photochemistry in the extra-tropical western North Pacific: Impact of continental outflow during the late winter/early spring. *Journal of Geophysical Research*, 102(D23), 28,469–28,487. <https://doi.org/10.1029/97JD02600>
- Ding, A., Wang, T., & Fu, C. (2013). Transport characteristics and origins of carbon monoxide and ozone in Hong Kong, South China. *Journal of Geophysical Research: Atmospheres*, 118, 9475–9488. <https://doi.org/10.1002/jgrd.50714>



- Ding, A. J., Fu, C. B., Yang, X. Q., Sun, J. N., Petäjä, T., Kerminen, V. M., et al. (2013). Intense atmospheric pollution modifies weather: A case of mixed biomass burning with fossil fuel combustion pollution in eastern China. *Atmospheric Chemistry and Physics*, 13(20), 10,545–10,554. <https://doi.org/10.5194/acp-13-10545-2013>
- Ding, A. J., Fu, C. B., Yang, X. Q., Sun, J. N., Zheng, L. F., Xie, Y. N., et al. (2013). Ozone and fine particle in the western Yangtze River Delta: An overview of 1 yr data at the SORPES station. *Atmospheric Chemistry and Physics*, 13(11), 5813–5830. <https://doi.org/10.5194/acp-13-5813-2013>
- Ding, A. J., Huang, X., Nie, W., Sun, J. N., Kerminen, V.-M., Petäjä, T., et al. (2016). Enhanced haze pollution by black carbon in megacities in China. *Geophysical Research Letters*, 43, 2873–2879. <https://doi.org/10.1002/2016GL067745>
- Ding, A. J., Nie, W., Huang, X., Chi, X., Sun, J., Kerminen, V.-M., et al. (2016). Long-term observation of air pollution-weather/climate interactions at the SORPES station: A review and outlook. *Frontiers of Environmental Science & Engineering*, 10(5), 15.
- Ding, A. J., Wang, T., Thouret, V., Cammas, J.-P., & Nedelec, P. (2008). Tropospheric ozone climatology over Beijing: Analysis of aircraft data from the MOZALC program. *Atmospheric Chemistry and Physics*, 8(1), 1–13. <https://doi.org/10.5194/acp-8-1-2008>
- Fishman, J., Ramanathan, V., Crutzen, P. J., & Liu, S. C. (1979). Tropospheric ozone and climate. *Nature*, 282(5741), 818–820. <https://doi.org/10.1038/282818a0>
- Fleming, Z. L., Doherty, R. M., von Schneidmesser, E., Malley, C. S., Cooper, O. R., Pinto, J. P., et al. (2018). Tropospheric ozone assessment report: Present-day ozone distribution and trends relevant to human health. *Elementa: Science of the Anthropocene*, 6(1), 12. <https://doi.org/10.1525/elementa.273>
- Fuhrer, J., Skarby, L., & Ashmore, M. R. (1997). Critical levels for ozone effects on vegetation in Europe. *Environmental Pollution*, 97(1–2), 91–106. [https://doi.org/10.1016/S0269-7491\(97\)00067-5](https://doi.org/10.1016/S0269-7491(97)00067-5)
- Geng, F. H., Zhang, Q., Tie, X. X., Huang, M. Y., Ma, X. C., Deng, Z. Z., et al. (2009). Aircraft measurements of O<sub>3</sub>, NO<sub>x</sub>, CO, VOCs, and SO<sub>2</sub> in the Yangtze River Delta region. *Atmospheric Environment*, 43(3), 584–593. <https://doi.org/10.1016/j.atmosenv.2008.10.021>
- Grell, G. A., Peckham, S. E., Schmitz, R., McKeen, S. A., Frost, G., Skamarock, W. C., & Eder, B. (2005). Fully coupled “online” chemistry within the WRF model. *Atmospheric Environment*, 39(37), 6957–6975. <https://doi.org/10.1016/j.atmosenv.2005.04.027>
- Guenther, A., Karl, T., Harley, P., Wiedinmyer, C., Palmer, P. I., & Geron, C. (2006). Estimates of global terrestrial isoprene emissions using MEGAN (Model of Emissions of Gases and Aerosols from Nature). *Atmospheric Chemistry and Physics*, 6(11), 3181–3210. <https://doi.org/10.5194/acp-6-3181-2006>
- Hawbaker, T. J., Radeloff, V. C., Syphard, A. D., Zhu, Z., & Stewart, S. I. (2008). Detection rates of the MODIS active fire product in the United States. *Remote Sensing of Environment*, 112(5), 2656–2664. <https://doi.org/10.1016/j.rse.2007.12.008>
- Huang, X., Ding, A., Liu, L., Liu, Q., Ding, K., Niu, X., et al. (2016). Effects of aerosol-radiation interaction on precipitation during biomass-burning season in East China. *Atmospheric Chemistry and Physics*, 16(15), 10,063–10,082. <https://doi.org/10.5194/acp-16-10063-2016>
- Huang, X., Li, M., Li, J., & Song, Y. (2012). A high-resolution emission inventory of crop burning in fields in China based on MODIS thermal anomalies/fire products. *Atmospheric Environment*, 50, 9–15. <https://doi.org/10.1016/j.atmosenv.2012.01.017>
- Huang, X., Wang, Z., & Ding, A. (2018). Impact of aerosol-PBL interaction on haze pollution: Multiyear observational evidences in North China. *Geophysical Research Letters*, 45, 8596–8603. <https://doi.org/10.1029/2018GL079239>
- Jiang, F., Guo, H., Wang, T. J., Cheng, H. R., Wang, X. M., Simpson, I. J., et al. (2010). An ozone episode in the Pearl River Delta: Field observation and model simulation. *Journal of Geophysical Research*, 115, D22305. <https://doi.org/10.1029/2009JD013583>
- Li, L., Chen, C. H., Huang, C., Huang, H. Y., Zhang, G. F., Wang, Y. J., et al. (2012). Process analysis of regional ozone formation over the Yangtze River Delta, China using the community multi-scale air quality modeling system. *Atmospheric Chemistry and Physics*, 12(22), 10,971–10,987. <https://doi.org/10.5194/acp-12-10971-2012>
- Li, M., Zhang, Q., Kurokawa, J. I., Woo, J. H., He, K., Lu, Z., et al. (2017). MIX: A mosaic Asian anthropogenic emission inventory under the international collaboration framework of the MICS-Asia and HTAP. *Atmospheric Chemistry and Physics*, 17(2), 935–963. <https://doi.org/10.5194/acp-17-935-2017>
- Li, X.-B., Wang, D., Lu, Q.-C., Peng, Z.-R., Fu, Q., Hu, X.-M., et al. (2018). Three-dimensional analysis of ozone and PM<sub>2.5</sub> distributions obtained by observations of tethered balloon and unmanned aerial vehicle in Shanghai, China. *Stochastic Environmental Research and Risk Assessment*, 32(5), 1189–1203. <https://doi.org/10.1007/s00477-018-1524-2>
- Lin, C. H., Lai, C. H., Wu, Y. L., Lai, H. C., & Lin, P. H. (2006). Vertical ozone distributions observed using tethered ozonesondes in a coastal industrial city, Kaohsiung, in southern Taiwan. *Environmental Monitoring and Assessment*, 127(1–3), 253–270.
- Lin, W., Xu, X., Ge, B., & Liu, X. (2011). Gaseous pollutants in Beijing urban area during the heating period 2007–2008: Variability, sources, meteorological and chemical impacts. *Atmospheric Chemistry and Physics*, 11(15), 8157–8170. <https://doi.org/10.5194/acp-11-8157-2011>
- Liu, H. Y., Chang, W. L., Oltmans, S. J., Chan, L. Y., & Harris, J. M. (1999). On springtime high ozone events in the lower troposphere from SE Asian biomass burning. *Atmospheric Environment*, 33(15), 2403–2410. [https://doi.org/10.1016/S1352-2310\(98\)00357-4](https://doi.org/10.1016/S1352-2310(98)00357-4)
- Mazzuca, G. M., Pickering, K. E., Clark, R. D., Loughner, C. P., Fried, A., Zweers, D. C., et al. (2017). Use of tethered sonde and aircraft profiles to study the mesoscale and microscale meteorology on air quality. *Atmospheric Environment*, 149, 55–69. <https://doi.org/10.1016/j.atmosenv.2016.10.025>
- McKee, D. J. (1994). *Tropospheric ozone: Human health and agricultural impacts* (pp. 9–18). New York: Lewis Publishers.
- Neu, U., Künzle, T., & Wanner, H. (1994). On the relation between ozone storage in the residual layer and daily variation in near-surface ozone concentration—A case study. *Boundary-Layer Meteorology*, 69(3), 221–247. <https://doi.org/10.1007/BF00708857>
- Nie, W., Ding, A. J., Xie, Y. N., Xu, Z., Mao, H., Kerminen, V. M., et al. (2015). Influence of biomass burning plumes on HONO chemistry in eastern China. *Atmospheric Chemistry and Physics*, 15(3), 1147–1159. <https://doi.org/10.5194/acp-15-1147-2015>
- Pan, X., Kanaya, Y., Tanimoto, H., Inomata, S., Wang, Z., Kudo, S., & Uno, I. (2015). Examining the major contributors of ozone pollution in a rural area of the Yangtze River Delta region during harvest season. *Atmospheric Chemistry and Physics*, 15(11), 6101–6111. <https://doi.org/10.5194/acp-15-6101-2015>
- Petzold, A., Thouret, V., Gerbig, C., Zahn, A., Brenninkmeijer, C. A. M., Gallagher, M., et al., & IAGOS TEAM (2015). Global-scale atmosphere monitoring by in-service aircraft—Current achievements and future prospects of the European research infrastructure IAGOS. *Tellus Series B: Chemical and Physical Meteorology*, 67(1), 28452. <https://doi.org/10.3402/tellusb.v67.28452>
- Petzold, A., Volz-Thomas, A., Thouret, V., Cammas, J.-P., & Brenninkmeijer, C. A. M. (2012). IAGOS—In-service Aircraft for a Global Observing System. In R. Sausen, S. Unterstrasser, & A. Blum (Eds.), *3rd international conference on Transport, Atmosphere and Climate* (Vol. Forschungs, pp. 69–76). Germany: Prien am Chiemsee. 25–28 June: Deutsches Zentrum für Luft- und Raumfahrt.
- Pollack, I. B., Ryerson, T. B., Trainer, M., Parrish, D. D., Andrews, A. E., Atlas, E. L., et al. (2012). Airborne and ground-based observations of a weekend effect in ozone, precursors, and oxidation products in the California South Coast Air Basin. *Journal of Geophysical Research*, 117, D00V05. <https://doi.org/10.1029/2011JD016772>

- Reitebuch, O., Strassburger, A., Emeis, S., & Kuttler, W. (2000). Nocturnal secondary ozone concentration maxima analysed by sodar observations and surface measurements. *Atmospheric Environment*, *34*(25), 4315–4329. [https://doi.org/10.1016/S1352-2310\(00\)00185-0](https://doi.org/10.1016/S1352-2310(00)00185-0)
- Schnell, R. C., Johnson, B. J., Oltmans, S. J., Cullis, P., Sterling, C., Hall, E., et al. (2016). Quantifying wintertime boundary layer ozone production from frequent profile measurements in the Uinta Basin, UT, oil and gas region. *Journal of Geophysical Research: Atmospheres*, *121*, 11,038–11,054. <https://doi.org/10.1002/2016JD025130>
- Schultz, M. G., Schröder, S., Lyapina, O., Cooper, O., Galbally, I., Petropavlovskikh, I., et al. (2017). Tropospheric ozone assessment report: Database and metrics data of global surface ozone observations. *Elementa: Science of the Anthropocene*, *5*, 58. <https://doi.org/10.1525/elementa.244>
- Spinhrne, J. D. (1993). Micro pulse lidar. *IEEE Transactions on Geoscience and Remote Sensing*, *31*(1), 48–55. <https://doi.org/10.1109/36.210443>
- Stein, A. F., Draxler, R. R., Rolph, G. D., Stunder, B. J. B., Cohen, M. D., & Ngan, F. (2015). NOAA's HYSPLIT atmospheric transport and dispersion modeling system. *Bulletin of the American Meteorological Society*, *96*(12), 2059–2077. <https://doi.org/10.1175/BAMS-D-14-00110.1>
- Stull, R. B. (1988). *An introduction to boundary layer meteorology*. Dordrecht; Boston; London: Kluwer; Academic Publishers, Springer. <https://doi.org/10.1007/978-94-009-3027-8>
- Sun, L., Xue, L. K., Wang, T., Gao, J., Ding, A. J., Cooper, O. R., et al. (2016). Significant increase of summertime ozone at Mount Tai in central eastern China. *Atmospheric Chemistry and Physics*, *16*(16), 10,637–10,650. <https://doi.org/10.5194/acp-16-10637-2016>
- Tang, H., Liu, G., Zhu, J., Han, Y., & Kobayashi, K. (2013). Seasonal variations in surface ozone as influenced by Asian summer monsoon and biomass burning in agricultural fields of the northern Yangtze River Delta. *Atmospheric Research*, *122*, 67–76. <https://doi.org/10.1016/j.atmosres.2012.10.030>
- Velasco, E., Márquez, C., Bueno, E., Bernabé, R. M., Sánchez, A., Fentanes, O., et al. (2008). Vertical distribution of ozone and VOCs in the low boundary layer of Mexico City. *Atmospheric Chemistry and Physics*, *8*(12), 3061–3079. <https://doi.org/10.5194/acp-8-3061-2008>
- Wang, R., Xu, X., Jia, S., Ma, R., Ran, L., Deng, Z., et al. (2017). Lower tropospheric distributions of O<sub>3</sub> and aerosol over Raoyang, a rural site in the North China Plain. *Atmospheric Chemistry and Physics*, *17*(6), 3891–3903. <https://doi.org/10.5194/acp-17-3891-2017>
- Wang, T., Cheung, V. T. F., Anson, M., & Li, Y. S. (2001). Ozone and related gaseous pollutants in the boundary layer of eastern China: Overview of the recent measurements at a rural site. *Geophysical Research Letters*, *28*(12), 2373–2376. <https://doi.org/10.1029/2000GL012378>
- Wang, T., Wei, X., Ding, A., Poon, C., Lam, K., Li, Y., et al. (2009). Increasing surface ozone concentrations in the background atmosphere of southern China, 1994–2007. *Atmospheric Chemistry and Physics*, *9*(16), 6217–6227. <https://doi.org/10.5194/acp-9-6217-2009>
- Wang, T., Xue, L., Brimblecombe, P., Lam, Y. F., Li, L., & Zhang, L. (2017). Ozone pollution in China: A review of concentrations, meteorological influences, chemical precursors, and effects. *Science of the Total Environment*, *575*, 1582–1596. <https://doi.org/10.1016/j.scitotenv.2016.10.081>
- Wang, Y., Konopka, P., Liu, Y., Chen, H., Muller, R., Ploger, F., et al. (2012). Tropospheric ozone trend over Beijing from 2002–2010: Ozone-sonde measurement and modeling analysis. *Atmospheric Chemistry and Physics*, *12*(18), 8389–8399. <https://doi.org/10.5194/acp-12-8389-2012>
- Wang, Z., Huang, X., & Ding, A. (2018). Dome effect of black carbon and its key influencing factors: A one-dimensional modeling study. *Atmospheric Chemistry and Physics*, *18*(4), 2821–2834. <https://doi.org/10.5194/acp-18-2821-2018>
- Wiedinmyer, C., Akagi, S. K., Yokelson, R. J., Emmons, L. K., Al-Saadi, J. A., Orlando, J. J., & Soja, A. J. (2011). The Fire INventory from NCAR (FINN): A high resolution global model to estimate the emissions from open burning. *Geoscientific Model Development*, *4*(3), 625–641. <https://doi.org/10.5194/gmd-4-625-2011>
- Xie, Y., Ding, A., & Nie, W. (2015). Enhanced sulfate formation by nitrogen dioxide: Implications from in situ observations at the SORPES station. *Journal of Geophysical Research: Atmospheres*, *120*, 679–712. <https://doi.org/10.1002/2015JD023607>
- Xing, C., Liu, C., Wang, S., Chan, K., Gao, Y., Huang, X., et al. (2017). Observations of the summertime atmospheric pollutants vertical distributions and the corresponding ozone production in Shanghai, China. *Atmospheric Chemistry and Physics*, *17*(23), 14,275–14,289. <https://doi.org/10.5194/acp-17-14275-2017>
- Xu, X., Lin, W., Wang, T., Yan, P., Tang, J., Meng, Z., & Wang, Y. (2008). Long-term trend of surface ozone at a regional background station in eastern China 1991–2006: Enhanced variability. *Atmospheric Chemistry and Physics*, *8*(10), 2595–2607. <https://doi.org/10.5194/acp-8-2595-2008>
- Xu, Z., Wang, T., Xue, L. K., Louie, P. K. K., Luk, C. W. Y., Gao, J., et al. (2013). Evaluating the uncertainties of thermal catalytic conversion in measuring atmospheric nitrogen dioxide at four differently polluted sites in China. *Atmospheric Environment*, *76*, 221–226. <https://doi.org/10.1016/j.atmosenv.2012.09.043>
- Xu, Z. N., Huang, X., Nie, W., Chi, X. G., Xu, Z., Zheng, L. F., et al. (2017). Influence of synoptic condition and holiday effects on VOCs and ozone production in the Yangtze River Delta region, China. *Atmospheric Environment*, *168*, 112–124. <https://doi.org/10.1016/j.atmosenv.2017.08.035>
- Xue, L. K., Wang, T., Gao, J., Ding, A., Zhou, X., Black, D. R., et al. (2014). Ground-level ozone in four Chinese cities: Precursors, regional transport and heterogeneous processes. *Atmospheric Chemistry and Physics*, *14*(23), 13,175–13,188. <https://doi.org/10.5194/acp-14-13175-2014>
- Zhang, J., & Rao, S. T. (1999). The role of vertical mixing in the temporal evolution of ground-level ozone concentrations. *Journal of Applied Meteorology*, *38*(12), 1674–1691. [https://doi.org/10.1175/1520-0450\(1999\)038<1674:TROVMI>2.0.CO;2](https://doi.org/10.1175/1520-0450(1999)038<1674:TROVMI>2.0.CO;2)
- Zhang, Y., Ding, A., Mao, H., Nie, W., Zhou, D. R., Liu, L. X., et al. (2016). Impact of synoptic weather patterns and inter-decadal climate variability on air quality in the North China Plain during 1980–2013. *Atmospheric Environment Part B Urban Atmosphere*, *124*, 119–128. <https://doi.org/10.1016/j.atmosenv.2015.05.063>
- Zheng, X. D., Chan, C. Y., Cui, H., Qin, Y., Chan, L., Zheng, Y. G., & Lee, Y. S. (2005). Characteristics of vertical ozone distribution in the lower troposphere in the Yangtze River Delta at Lin'an in the spring of 2001. *Science in China-Series D*, *48*(9), 1519. <https://doi.org/10.1360/03yd0492>
- Zhou, D. R., Ding, A., Mao, H., Fu, C., Wang, T., Chan, L. Y., et al. (2013). Impacts of the East Asia monsoon on lower tropospheric ozone over coastal south China. *Environmental Research Letters*, *8*(4), 044011. <https://doi.org/10.1088/1748-9326/8/4/044011>
- Zhu, B., Kang, H. Q., Zhu, T., Su, J., Hou, X., & Gao, J. (2015). Impact of Shanghai urban land surface forcing on downstream city ozone chemistry. *Journal of Geophysical Research: Atmospheres*, *120*, 4340–4351. <https://doi.org/10.1002/2014JD022859>